Utrecht University

Debye Institute for Nanomaterials Science

Nanophotonics Group

Thermalization and Effective Interactions in Photon Condensates

Author:
C. Beulenkamp BSc

Supervisor:
dr. D. van Oosten

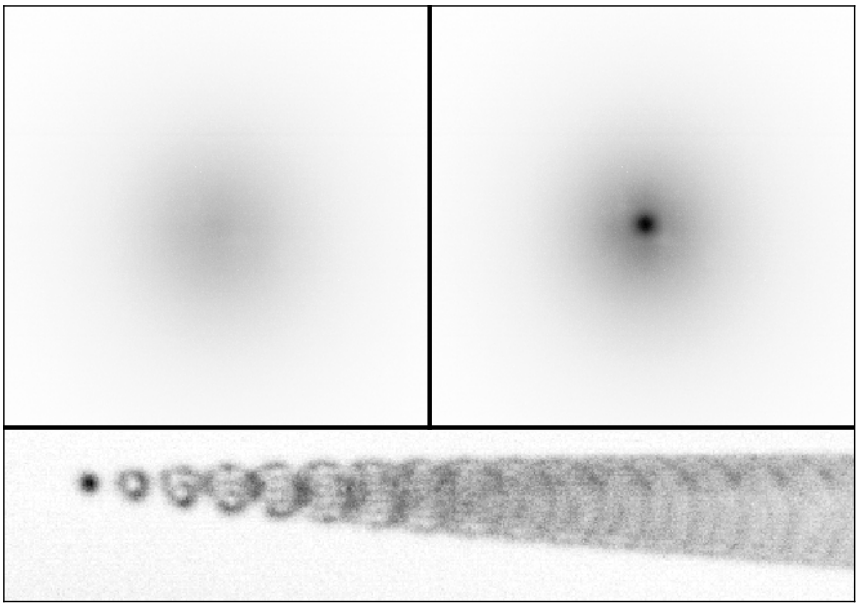

June 27, 2018

Abstract

The experimental realization of a Bose-Einstein condensate of photons, first achieved in 2010 at Bonn University, allowed for new ways to probe the properties of condensates. For thermal light in free space the chemical potential is zero and condensation is not possible. By confining light to a microcavity, the transverse degrees of freedom behave as massive bosons which can have nonzero chemical potential. The gas of thermal photons can be brought to thermalize with a fluorescent dye though absorption and emission cycles. By pumping the dye molecules with a laser, the chemical potential can be increased and the photons will condense.

We have built a setup with which we can spatially and spectrally resolve the photon distribution in such a dye-filled microcavity. This allows us to study the shape and occupation of the low energy transverse modes of the cavity. We use this to investigate the thermalization process of the photon gas. A rate equation model is presented and qualitatively compared to experimental data. We find that the photon gas is not in thermal equilibrium.

We also investigate effective photon-photon interactions by measuring the spatial extent of the condensate. We find an effective interaction in the form of thermal lensing. As the thermal lensing depends on the interaction between the photon gas and the dye, we find that the model used for thermalization can also make good predictions about effective photon-photon interactions.

Acknowledgements

I'd like to thank Dries van Oosten for supervising me and letting me off the leash. Having complete control over the setup was intimidating at first, but I liked the freedom it gave me to play around. Being able to improvise with whatever I could find in the closet when iterating on a setup has greatly increased my intuition when it comes to optics. Of course, this would not be possible without the help of Sebastiaan Greveling, who built the original setup, instructed me on how to use it and fixed things when they broke. I also want to thank Maarten Droste, who worked on simulations of the rate equation model, which allowed me to make more progress in my understanding of both the model and the experimental results. Discussions on fitting techniques and Rhodamine dye with Allard Mosk were also very helpful. I'd also like to thank the technicians Cees de Kok, Dante Kilian and Paul Jurrius for technical support on the setup.

Lastly I would like to thank everyone at Nanophotonics for interesting and/or stupid discussions. Jasper for talking during lunch so I didn't have to, Mijke for not shooing me away when I walked into her office for no particular reason, Javi for enduring my taste in music and countless other who I can't think of right now because I'm not good at writing acknowledgements

Contents

1 Introduction

Shortly after the development of boson statistics by Bose in 1924 [1], Einstein applied these statistics to atomic gases [2]. He found that at high phase space densities bosons would condense into a macroscopic occupation of the ground state. This phenomenon is now known as Bose-Einstein condensation. Reaching sufficiently high phase space densities requires extremely low temperatures and/or high densities. Because of these experimental challenges it took until 1995 for the first Bose-Einstein condensates, consisting of 5×10^5 sodium atoms, to be created in a laboratory [3]. The realization of Bose Einstein condensation allowed the study of quantum mechanical effects on a macroscopic scale.

In the years since the first Bose-Einstein condensate many more types of bosons have been condensed. Isotopes of various atoms, molecules and quasiparticles like magnons [4] or polaritons [5]. In all of these systems, the system has to thermalize and particles are lost over time. When the thermalization time is much shorter than the lifetime, the system can be accurately described by considering it to be in thermal equilibrium. For atoms confined in magnetic traps the lifetimes are far larger than the thermalization time and thermal equilibrium can be assumed. For quasiparticles with short lifetimes, such as the polariton, particles need to be continuously added to maintain the densities necessary for condensation. These are thus driven-dissipative systems, better described using a master equation than a Hamiltonian. Condensates of photons, the subject of this thesis, are somewhere in between these two regimes.

To achieve Bose-Einstein condensation of light, one has to start with a thermal gas of photons. For thermal light in free space the number of photons is not conserved. Lowering the temperature reduces the number of photons, making condensation impossible. An alternative was found by Chiao *et al* [6], who confined light to a microcavity. By fixing the longitudinal wavenumber the photons behave as massive particles in 2 dimensions. The group of Martin Weitz expanded on this by adding a fluorescent dye to which the photon gas would thermalize [7] and achieved condensation in 2010 [8]. Similar setups were built in London in 2014 and in our group in Utrecht in 2015.

Outline

Chapter 2 covers the basic concepts necessary for photon condensation in dye filled cavities. Chapter 3 explains the setup with which we condense light and some of the methods which we use to analyse the light leaking out of the cavity. Chapter 4 discusses theory on how the dye-photon interaction thermalizes the photon gas and compares a rate equation model to some experimental results. Chapter 5 presents measurements of the effective photon-photon interactions and compares them to previous experiments. We then interpret the results using concepts from our treatment of the thermalization. Chapter 6 gives suggestions for future research. Appendix A is a glossary of the symbols and constants used in this thesis, with numerical values given where possible. Appendix B gives details on the data presented in this thesis and how each dataset was processed.

2
Bose-Einstein Condensation of Photons

This chapter covers the basics of photon condensation in microcavities. First we will show how confinement in the cavity gives the photons an effective rest mass by removing one degree of freedom and how the curvature of the mirrors leads to a harmonic trap in 2 dimensions. The thermalization mechanism of the photons will then be described, and Bose-Einstein condensation in 2D will be treated. Finally we will see how these come together in an experimental realization of photon condensation and recast some of the formulas in terms of measurable quantities.

2.1 Trapped massive photons

A cavity can be used to trap photons with a fixed wavenumber along the cavity axis. The dispersion relation for the remaining degrees of freedom is approximately that of a massive free particle moving in 2 dimensions. If the mirrors are curved the particles feel an effective potential as well. To see this, consider the energy of a photon with wavenumber k_z along the cavity axis and wavenumber $\mathbf{k}_\perp$ perpendicular to it

$$E_{ph} = \frac{\hbar c}{n_0}\sqrt{k_z^2 + \mathbf{k}_\perp^2}. \tag{2.1}$$

By setting Dirichlet boundary conditions such that the electromagnetic field vanishes on the surface of the mirrors we fix the longitudinal wave number

$$k_z(\mathbf{r}) = \frac{q\pi}{D(\mathbf{r})}, \tag{2.2}$$

where q is a positive integer known as the mode number and $D(r)$ is the cavity length at position $\mathbf{r}$, which in the case of perfectly aligned spherical mirrors with a radius of curvature R is given by

$$D(\mathbf{r}) = D_0 - 2(R - \sqrt{R^2 - \mathbf{r}^2}). \tag{2.3}$$

Using the paraxial approximation $k_z \gg k_\perp$ and $R \gg |\mathbf{r}|$ we can expand the energy as

$$E_{ph}(\mathbf{r}) \approx m_{ph}\left(\frac{c}{n_0}\right)^2 + \frac{(\hbar\mathbf{k}_\perp)^2}{2m_{ph}} + \frac{1}{2}m_{ph}\Omega^2\mathbf{r}^2, \tag{2.4}$$

where n_0 is the refractive index inside the cavity and the effective photon mass is

$$m_{ph} = \frac{n_0\hbar}{c}k_z(0) = \frac{n\hbar}{c}\frac{q\pi}{D_0} \tag{2.5}$$

and the trap frequency is

$$\Omega = \frac{c}{n_0}\sqrt{\frac{2}{D_0 R}}. \tag{2.6}$$

The photons thus behave like massive bosons in a 2 dimensional harmonic trap. By seperating it into two 1 dimensional harmonic oscillators with quantum numbers $\mathbf{m} = (m_x, x_y)$ we find that the eigenenergies are given by $E_{\mathbf{m}} = \hbar\Omega(m_x + m_y + 1)$ and the corresponding eigenstates are

$$\psi_{\mathbf{m}}(\mathbf{r}) = \frac{H_{m_x}(\frac{x}{l_{\mathrm{HO}}})H_{m_y}(\frac{y}{l_{\mathrm{HO}}})e^{-\frac{x^2+y^2}{2l_{\mathrm{HO}}^2)}}}{l_{\mathrm{HO}}^2\sqrt{\pi 2^{m_x+m_y}m_x!m_y!}}, \tag{2.7}$$

where $l_{\mathrm{HO}} = \sqrt{\hbar/m_{\mathrm{ph}}\Omega}$ is known as the harmonic oscillator length. For a fixed mode number q there are no states below the ground state $\omega_c = (m_{ph}/\hbar)(c/n_0)^2 + \Omega$, which is therefore referred to as the cutoff frequency. This is the frequency where the condensate will form and, as we will see in Chapter 4, its value will affect the thermalization of the photon gas.

2.2 Thermalization of light

To thermalize the two dimensional photon gas the cavity is filled with a solution of Rhodamine 6G, a fluorescent dye. The spectrum of this dye is plotted in Fig. 2.1a. The energy levels of this molecule can be modeled as a two level system with the ground and excited states split into bands due to the rovibrational modes of the molecule. These bands are commonly referred to as S_0 and S_1 respectively. When a dye molecule is excited by the absorption of a photon it thermalizes inside the upper band on a subpicosecond timescale due to dye-solvent collisions. (see Fig. 2.1b) Due to this thermalization the Einstein coefficients for absorption $B_{12}(\omega)$ and emission $B_{21}(\omega)$ obey the Kennard-Stepanov relation [9] [10] [11]

$$B_{21}(\omega)/B_{12}(\omega) \propto e^{-\beta\hbar(\omega-\omega_{\mathrm{ZPL}})}, \tag{2.8}$$

where $\beta = (k_B T)^{-1}$ and ω_{ZPL} is the zero-phonon line, the frequency of the transition between the ground and excited states of the molecule in absence of rovibrational modes. To see how this leads to a thermal photon gas, consider the rate $R(\mathbf{m} \to \mathbf{m'})$ of a photon going from state $\mathbf{m}$ to $\mathbf{m'}$. This rate is proportional to $B_{21}(\omega_{\mathbf{m}})B_{12}(\omega_{\mathbf{m'}})$, so the ratio of the rates going to $\mathbf{m'}$ from $\mathbf{m}$ and vice versa is:

$$\frac{R(\mathbf{m} \to \mathbf{m'})}{R(\mathbf{m'} \to \mathbf{m})} = \frac{B_{21}(\omega_{\mathbf{m}})B_{12}(\omega_{\mathbf{m'}})}{B_{21}(\omega_{\mathbf{m'}})B_{12}(\omega_{\mathbf{m}})} = e^{-\beta\hbar(\omega_{\mathbf{m}}-\omega_{\mathbf{m'}})}. \tag{2.9}$$

Given enough time the flow of particles between different states will balance out, leading to the probability to find the photon in state $\mathbf{m}$ given by $P(\omega_{\mathbf{m}}) = e^{-\beta\hbar(\omega_{\mathbf{m}}-\omega_c)}$. The photons thus settle into a thermal distribution.

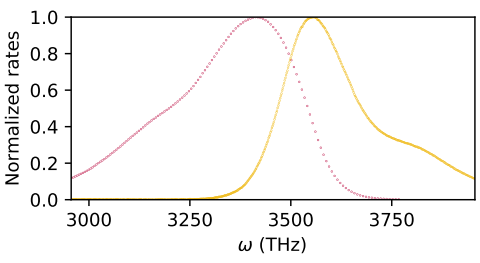

(a) The normalized absorption and emission spectra of Rhodamine 6G [12]

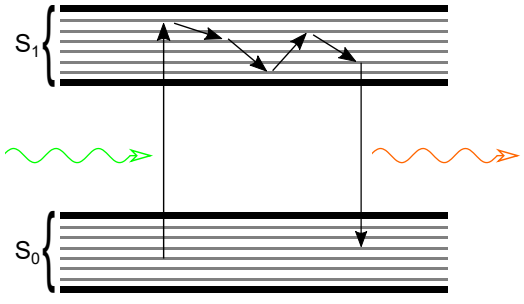

(b) Diagram showing the process of photon thermalization.

2.3 Condensation in the ideal Bose gas

Now that we have established that we can thermalize quasiparticles inside a cavity, we can see how Bose-Einstein condensation occurs for bosons in 2D. In a system with temperature T and chemical potential μ, the thermal expectation value for the occupation of a bosonic state with energy ϵ is given by the Bose-Einstein distribution

$$f(\epsilon) = \frac{1}{e^{\beta(\epsilon-\mu)} - 1}. \tag{2.10}$$

Condensation occurs when the chemical potential approaches the energy ϵ_0 of the ground state and $f(\epsilon_0)$ diverges. The chemical potential can be increased by adding particles while holding the temperature fixed. To see how many particles we need to add, we can compute the total number of particles at $\epsilon_0 - \mu = 0$. This number can be found by summing the expectation values of every state. In the limit where the spacing between energy levels is much smaller than $k_B T$, the sum over the excited states can be approximated by an integral

$$N_{ex} = \int_0^\infty f(\epsilon) D(\epsilon) d\epsilon. \tag{2.11}$$

where $D(\epsilon)$ is the density of states. We can take the density of states to be $D(\epsilon) = D\epsilon^{p-1}$. Then the number of particles in the excited states is

$$N_{ex} = D \int_0^\infty \frac{\epsilon^{p-1}}{e^{\beta(\epsilon-\mu)} - 1} d\epsilon = D\zeta(p)\Gamma(p), \tag{2.12}$$

where $\zeta(p)$ is the Riemann zeta function, and $\Gamma(p)$ is the Gamma function, which are defined as

$$\zeta(p) = \sum_{k=1}^{\infty} \frac{1}{k^p}, \qquad \Gamma(p) = \int_0^\infty dx x^{p-1} e^{-x}. \tag{2.13}$$

When $p > 1$, N_{ex} is a finite positive number, and thus condensation is possible.

For the uniform bose gas in 2D we find that $p = 1$, so condensation is not possible. The harmonic trapping due to the curvature of the mirrors changes the density of states to

$$D(\epsilon) = N_S \frac{\epsilon}{(\hbar\Omega)^2}. \tag{2.14}$$

with N_S being the number of spin degrees of freedom. In this case condensation is possible and occurs above the critical photon number

$$N_C = N_S \frac{\pi^2}{6} \left(\frac{k_B T}{\hbar\Omega} \right)^2. \tag{2.15}$$

Because it is not possible to add more particles to the excited states by increasing the total number of particles, the thermal cloud is said to be saturated. The number of particles in the ground state is then

$$N_0 = N_{tot} - N_C. \tag{2.16}$$

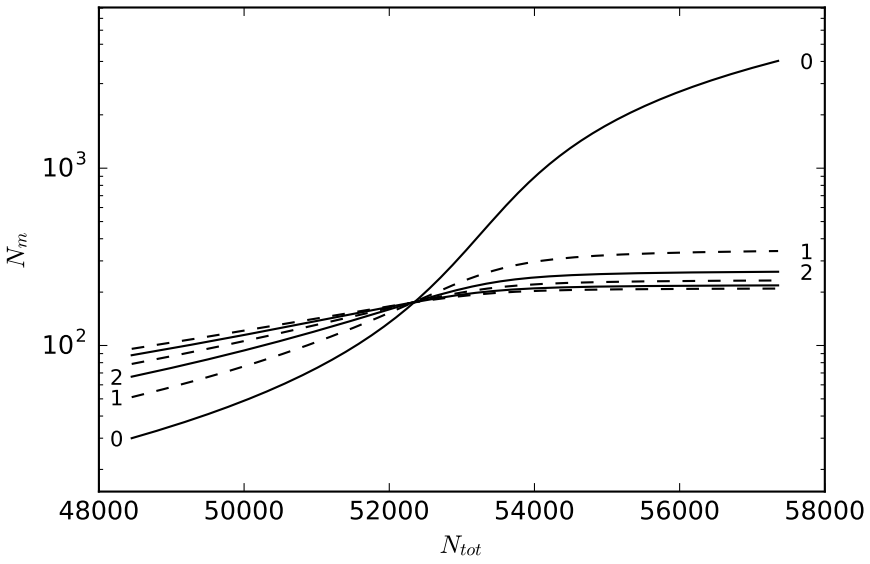

Figure 2.2: Occupations of the first few energy levels as a function of the total number of particles, with $N_S = 1$.

At energies much smaller than k_BT, the Bose-Einstein distribution can be approximated by the Rayleigh-Jeans law

$$f(\epsilon) \approx \frac{k_BT}{\epsilon - \mu}. \tag{2.17}$$

As the degeneracy of energy level $E_m = \hbar\Omega(m+1)$ is $g_m = m+1$, the expected number of particles with this energy can then be written as

$$N(E_m) \approx N_S \frac{k_BTg_m}{E_m - \mu} = N_S \frac{k_BT}{\hbar\Omega} \frac{m+1}{(m+1) - \mu/\hbar\Omega}. \tag{2.18}$$

Fig. 2.2 shows how the occupations of the energy levels behave around the condensation threshold. When μ is negative, $n_m > n_{m'}$ if $m > m'$. At $\mu = 0$ the levels are equally occupied. As μ approaches $E_0 = \hbar\Omega$, the occupation of the ground state diverges and the occupations of the excited states become fixed at $n_m = N_S \frac{k_BT}{\hbar\Omega} \frac{m+1}{m}$, which again shows the saturation of the excited states.

2.4 Experimental realization and terminology

The above derivations are all based on simplifying assumptions. In experiments there are a number of things complicating things. Photons are lost due to nonradiative decays of due molecules and transmission though the mirrors. Therefore, to maintain high enough photon numbers for condensation, more photons must be continuously added. This is achieved by exciting the dye molecules using a pump laser. The light leaking through the mirrors can however be used to study the intracavity photon distribution. This means that, in contrast to most experiments on atomic BECs, one does not have to further disturb the photon BEC to do measurements.

3 Setup and Methods

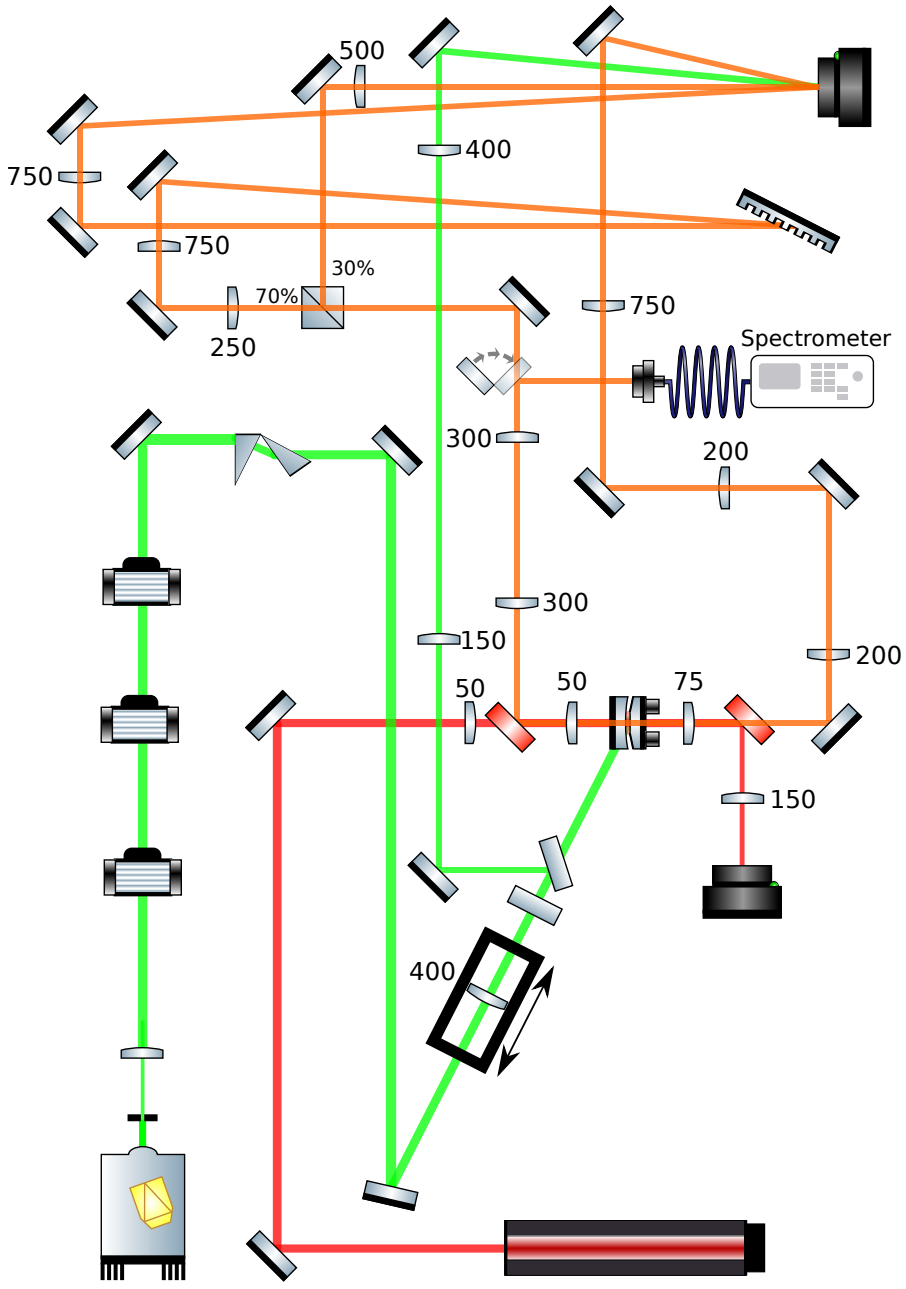

Figure 3.1: Schematic setup, some mirrors have been omitted and distances are not to scale

3.1 Experimental setup

Fig. 3.1 shows a schematic depiction of our setup. The elements of the setup can be grouped into the following categories: the dye cavity, the pump laser and the imaging system. There is also a setup for measuring the polarization of the photon distribution [13], which was not used for the work presented here.

3.1.1 The microcavity

The microcavity consists of two high reflectivity mirrors (CRD Optics, 901-0010-0550) with a radius of curvature of 1 meter. One of the mirrors is ground down to a cone topped with a small mirror of diameter of 1.5 mm. The cavity length can be varied by hand using a translation stage. The small mirror is mounted on piezo actuators allowing for fine control of the cavity length and transverse displacement. In between the two mirror is a droplet of Rhodamine 6G dissolved in ethylene glycol, which is held in place by capillary forces. Before starting experiments, the cavity is opened and the mirrors are cleaned with First Contact Polymer. A new droplet of dye solution is then added. To maintain a constant cavity length during experiments, a feedback mechanism is used. This cavity locking utilizes a Helium neon (HeNe) laser at 632.8 nm. The light from this laser passes through the cavity only at the positions where the cavity length is a multiple of the HeNe light wavelength. This leads to circular patterns known as Newton rings. The HeNe light is split off using a dichroic mirror and imaged onto a CCD camera (Point Grey Flea FL3-U3-13Y3M). The radius of the innermost Newton ring is determined by a fast fitting procedure. The radius is kept constant by applying a feedback signal to the piezos, thus stabilizing the cavity length.

3.1.2 Pump laser

The dye inside the cavity is pumped using pulses from a 532 nm CW laser (Laser Quantum Gem 532). The laser beam is passed through three acousto-optical modulators (AOMs), which chop the beam into pulses with a duration of approximately 500 ns. The first AOM is used to control the pulse power and the second and third are used to improve the extinction ratio.

The pump beam is aligned such that it enters the cavity at an angle of 65 degrees to maximize transmission. This causes the horizontal width of the pump spot to be enlarged by a factor of $1/\cos(65°) = 2.36$. To compensate for this, the beam is expanded in the vertical direction using an anamorphic prism pair. A lens positioned in a zoom housing creates a focus that can be moved to change the size of the pump beam at the cavity. Following the lens, the beam goes through a glass plate mounted in a mirror mount. By rotating the glass plate the beam can be displaced by small distances, allowing for fine control over the pump spot position. A beam sampler then splits off a few percent of the beam to be used to image the pump spot before the rest of beam enters the cavity.

3.1.3 Imaging

Imaging is done using a Zyla 5.5 sCMOS camera. The integration time is set to 200 µs. A measurement produces two images, one containing the image of the cavity light during the pump pulse and one image of background light which is subtracted from the first image. To not waste storage space, we only read out a part of the chip 800 pixels high. This region is divided into four regions, each containing a different image. An example of a measurement can be seen in Fig. 3.2.

The light leaking from the large mirror is split into two paths. Thirty percent is used to directly image the cavity with a magnification of $M_L = 10$ (Fig. 3.2b). The other seventy percent is used to make a spectrally resolved image with a magnification of $M_S = 5$ using an echelle grating with a groove density of 79 lines/mm and a blaze angle of 63 degrees (Fig. 3.2a). Light exiting through the small mirror is imaged on the Zyla with a magnification of $M_S = 10$ (Fig. 3.2c). Because the beam sampler is the last element the pump pulse goes through before entering the cavity, the split off signal contains full information about the pump spot, e.g. location, size, intensity. The split off part of the pump laser is imaged onto the Zyla with a magnification of $M_P = 400/150 = 2.67$ with respect to the pump spot size at the cavity (Fig. 3.2d). Note that the image of the pump spot does not undergo the anamorphic magnification caused by the 65 degree angle of incidence.

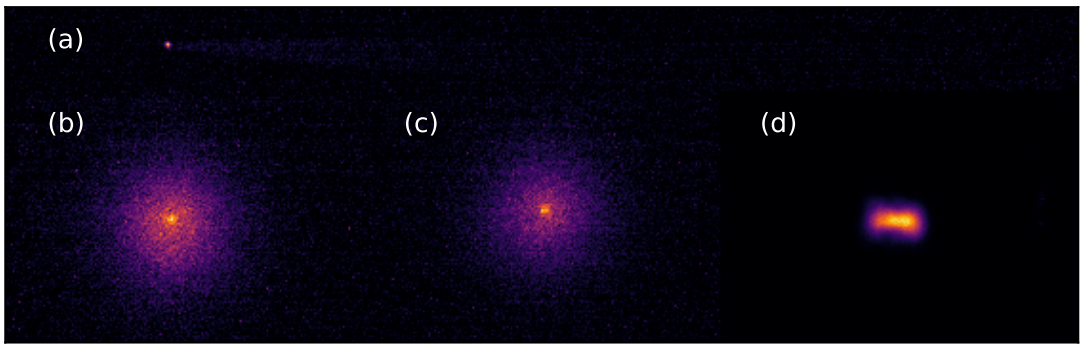

Figure 3.2: An example of a measurement with the background subtracted. The four images are normalized so that the signal is visible. They are: (a) the spectrum, (b) the image coming through the large mirror, (c) the image coming through the small mirror and (d) the image of the pump spot.

3.1.4 Calibration

When doing theory it is convenient to use the cutoff wavelength, but in experiments we work with the cutoff wavelength $\lambda_c = \frac{2\pi c}{\omega_c}$. Note that this is the wavelength in air corresponding to the cutoff frequency, not the longitudinal wavelength of the modes inside the cavity. The cutoff wavelength can be measured by redirecting the light leaking from the large mirror into a fiber spectrometer (Ocean Optics, HR2000CG-UV-NIR) using a flip mirror. The Newton rings used for cavity locking can be imaged by removing the notch filter in the imaging path for the small mirror. By measuring the radius of the inner ring and the corresponding cutoff wavelength at two different points we can determine the mode number q using

$$D(r_1) - D(r_2) \approx \frac{r_2^2 - r_1^2}{R} = \frac{q}{2}\frac{\lambda_1 - \lambda_2}{n_0}. \tag{3.1}$$

Because the angle of incidence onto the echelle grating is not the same as the angle of reflection the collimated beam will be slightly wider after passing the grating. This leads to a narrowing in the image. This narrowing only occurs in the plane of incidence, so the spectrally resolved images will end up with an anamorphic magnification. To determine the anamorphic magnification we measure the aspect ratio of the Newton rings for the two diffraction orders of HeNe light surrounding the diffraction order of the condensate light and take the average to be the anamorphic magnification. It was found to be 0.908 ± 0.013. Whilst the imaging systems of the small mirror and the large mirror are both 4f systems, the imaging system for the spectrum is not. To characterize possible aberrations in the magnification resulting from this we compare the size of the Newton rings in the spectrally resolved image and the normal images. Assuming the magnification of the image of the large mirror to be exactly 10, we find that the magnification for the spectrally resolved image is 4.971 ± 0.05.

3.2 Data analysis

When processing a dataset we determine for every image:

- The run and frame.
- The total number of counts in the images of the pump spot and the large and small mirrors.
- The best fit parameters acquired by fitting the probability distribution of the harmonic oscillator ground state to the image of the ground state in the spectrum.
- The total number of counts in the area where the fitting procedure determined the ground state to be.
- The total number of counts in an area slightly to the left of the ground state, which corresponds to a wavelength below the cutoff wavelength.

The most important of these is the fit to the ground state, which has to deal with low signal to noise when fitting images of the photon distribution below threshold. Once these quantities are determined, measurements with failed fits are filtered out. In Appendix B details can be found about each dataset, including the filtering criteria.

3.2.1 Fitting the ground state

The fit to the ground state is very sensitive to the initial values, as higher order modes also have a roughly Gaussian shape which will lead to a local minimum for a least squares fitting procedure. It is therefore important to determine accurately where in the image the image of the ground state is. The cavity locking method we use does not stabilize the cutoff frequency to within the splitting Ω between the ground state and the first excited states, which means that the position of the ground state has to be determined for each measurement. The experiments presented in this thesis consist of 20000 or more measurements, so finding the ground state can not be done by hand. We therefore apply the following procedure, visually represented in Fig. 3.3, to find the ground state for each measurement:

a. Take the part of the image that contains the spectrum.

b. Apply a Gaussian blur with a kernel of 5 pixels to smoothen out noise.

c. Sum over the y-axis in a range in which the condensate can be found (usually about 20 pixels high) and find peaks in the resulting 1D array using scipy's `find_peaks_cwt`.

d. Take the position of the left most peak as x_{fit} and find the y coordinate such that $I(x_{\text{fit}}, y)$ is maximal. Take this as y_{fit} Crop the image to a square with $(x_{\text{fit}}, y_{\text{fit}})$ as its center.

e. Fit the ground state distribution to this cropped image. The crop significantly reduces computation time and prevents higher order modes from affecting the fit to the ground state.

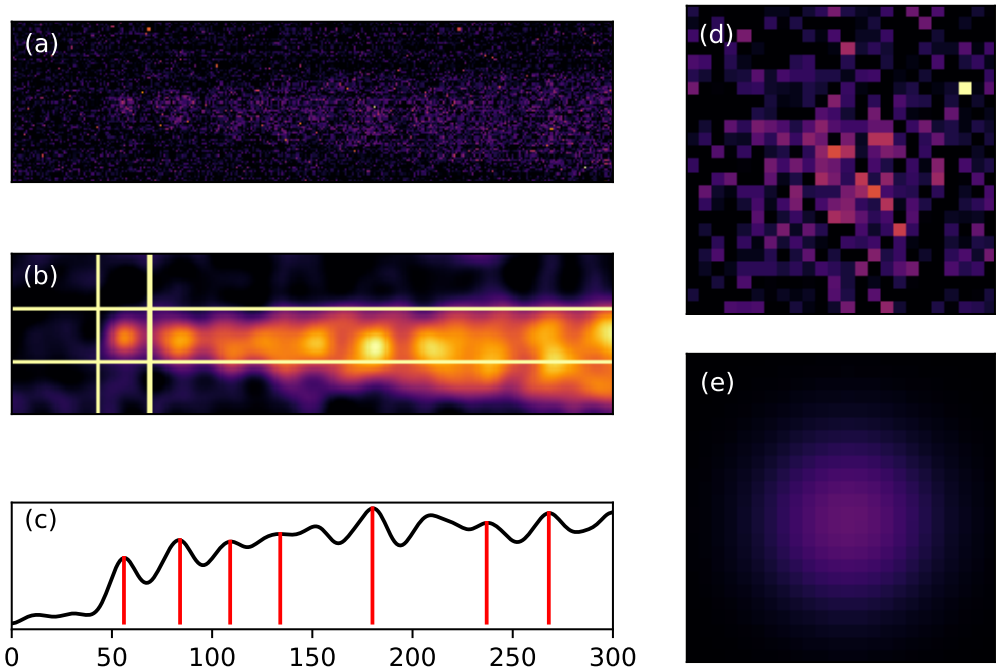

Figure 3.3: Images of the steps in the fitting procedure.
Subfigure (a) shows the data we want to fit. Subfigure (b) shows the data after a Gaussian blur is applied. The final square used for fitting is also marked. Subfigure (c) is the vertically binned data, with peaks marked by red lines. Subfigure (d) is the cropped square to which we fit the ground state distribution. Subfigure (e) is the best fit.

Fitting errors

When the signal to noise of the images is low, there will be systematic errors in the best fit parameters. To examine possible photon-photon interactions we need to accurately determine the size of the condensate. To eliminate the possibility that we identify a fitting error as a physical process, we have examined this error numerically.

First, images are generated that simulate experimental data. A total of 10000 images are produced. The starting point is an image of 50 by 50 pixels with all values set to 200 counts, which represents background light. A 2D Gaussian distribution is then added, with the center being at $(25 + dx, 25 + dy)$, where dx, dy are random numbers in the interval $[0, 1]$. The widths are fixed at 7 pixels in the x-direction and 6 pixels in the y-direction. The sum over the Gaussian is set to be equal to the number of the generate image, e.g. the sum over picture 200 is equal to 200. This distribution is then subjected to Poisson noise, and a background image with Poisson noise is subtracted. The generated images are fitted using the same fitting procedure as for experimental data. The data is binned according to the number of counts and the weighted average of the width for each bin is computed.

Fig. 3.4 shows the errors in the best fit widths as a function of the total number of counts. As one decreases the total counts the fit deteriorates because peaks in the noise become more significant than the signal. The relative errors mark the smallest change in width that can be seen as significant, i.e. resulting from physical phenomena rather than numerical ones in our analysis.

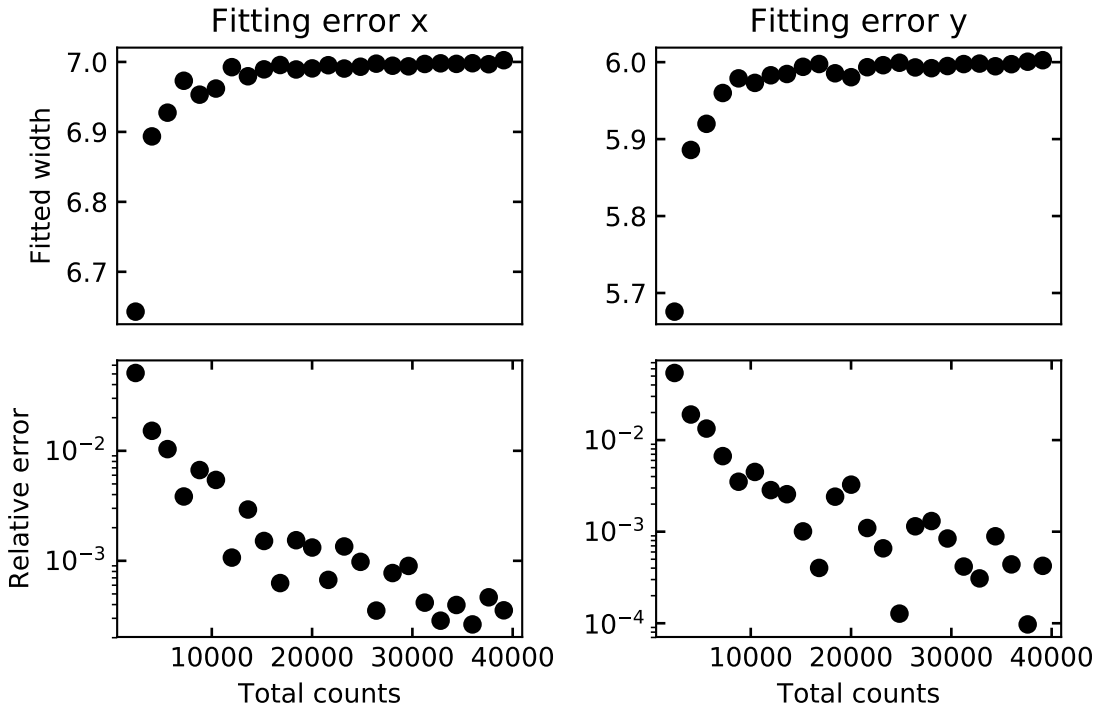

Figure 3.4: Best fit widths. The top graphs show the weighted averages and the bottom graphs show the absolute error expressed in terms of the real width of the distribution.

4 Photon thermalization and multimode condensation

4.1 Introduction

The observation of photon condensation drew comparisons to polariton condensates. It was necessary to establish a distinction between lasing and condensation through thermalization. This distinction was made in two papers by Peter Kirton and John Keeling [14] [15], where they examined the thermalization and condensation of the photon gas in a nonequilibrium model. Experimental observations of pump dependent effects and multimode condensation [16] [17] prompted an extension of the model with a dye excitation field depending on position [18]. We will here compare the predictions of this model with some experimental results, in particular the spectrum of the photon gas. We will first present the rate equation model and see what kind of predictions it makes. We will then look at some experimental results and interpret them using the concepts from the model.

4.2 Theory: the rate equation model

Kirton and Keeling first performed an adiabatic elimination of the rovibrational states so that that the dye could be treated as a two level system [14]. From the master equation they then reduced the problem to a set of rate equations by assuming coherence between different modes to be negligible. This assumption is not strictly correct, as emission into wave packets has been observed experimentally [17], but it reduces the amount of equations significantly. This makes it possible to examine steady state solutions in some cases and to solve the problem numerically. The rate equations are a set of coupled equations relating time evolution of the mode occupations $N_{\mathbf{m}} = \langle a^\dagger_{\mathbf{m}} a_{\mathbf{m}} \rangle$ and the local excitation density $f(\mathbf{r})$, which is the local fraction of excited dye molecules.

$$\partial_t N_{\mathbf{m}} = -\kappa N_{\mathbf{m}} + \rho_0 f_{\mathbf{m}} \Gamma^{(\mathbf{m})}_{\downarrow}(N_{\mathbf{m}} + 1) - \rho_0(1 - f_{\mathbf{m}})\Gamma^{(\mathbf{m})}_{\uparrow} N_{\mathbf{m}}, \tag{4.1}$$

$$\partial_t f(\mathbf{r}) = -\Gamma^{\mathrm{tot}}_{\downarrow}(\{N_m\}, \mathbf{r}) f(\mathbf{r}) + \Gamma^{\mathrm{tot}}_{\uparrow}(1 - f(\mathbf{r})), \tag{4.2}$$

$$\Gamma^{\mathrm{tot}}_{\downarrow}(\{N_{\mathbf{m}}\}, \mathbf{r}) = \Gamma_{\downarrow} + \Sigma_{\mathbf{m}} |\psi_{\mathbf{m}}(\mathbf{r})|^2 \Gamma^{(\mathbf{m})}_{\downarrow}(N_{\mathbf{m}} + 1), \tag{4.3}$$

$$\Gamma^{\mathrm{tot}}_{\uparrow}(\{N_{\mathbf{m}}\}, \mathbf{r}) = \Gamma_{\uparrow}(\mathbf{r}) + \Sigma_{\mathbf{m}} |\psi_{\mathbf{m}}(\mathbf{r})|^2 \Gamma^{(\mathbf{m})}_{\uparrow} N_{\mathbf{m}}. \tag{4.4}$$

Eq. 4.1 governs the mode occupations $N_{\mathbf{m}}$, with the first term on the right hand side accounting for cavity losses at a rate κ and the second and third terms representing emission and absorption respectively. Here, ρ_0 is the number density of dye molecules, $\Gamma^{(\mathbf{m})}_{\downarrow}$ is the

emission rate for mode $\mathbf{m}$ and $\Gamma_{\uparrow}^{(\mathbf{m})}$ is the absorption rate for mode $\mathbf{m}$. The number $f_{\mathbf{m}}$ is defined as the overlap between mode $\mathbf{m}$ and $f(\mathbf{r})$ i.e. $f_{\mathbf{m}} = \int d^2\mathbf{r} f(\mathbf{r})|\psi_{\mathbf{m}}(\mathbf{r})|^2$. We can thus interpret $\rho_0 f_{\mathbf{m}}$ as the sun over all excited dye molecules weighted by their coupling to mode $\mathbf{m}$. The time evolution of the excitation density $f(\mathbf{r})$ is governed by Eq. 4.2, with the excitation density being increased by the excitation rate $\Gamma_{\uparrow}^{\text{tot}}(\{N_m\}, \mathbf{r})$ and decreased by the decay rate $\Gamma_{\downarrow}^{\text{tot}}(\{N_m\}, \mathbf{r})$. The excitation rate Eq. 4.4 is the sum of absorption of pump light $\Gamma_{\uparrow}(\mathbf{r})$ and absorption of cavity photons. The decay rate Eq. 4.3 is a sum of non-cavity emission $\Gamma_{\downarrow}$ and emission into the cavity modes. In this notation the Kennard-Stepanov relation can takes the form $\Gamma_{\uparrow}^{(\mathbf{m})} = \Gamma_{\downarrow}^{(\mathbf{m})} e^{\beta\hbar\delta_{\mathbf{m}}}$, where $\delta_{\mathbf{m}} = \omega_{\mathbf{m}} - \omega_{\text{ZPL}}$ is the detuning from the zero-phonon line.

These rate equations can be solved numerically and give insight into the way the photon distribution deviates from a thermal distribution. An extension of the model which added proper treatment of polarization states to the model [19] found that when the pump is linearly polarized, the polarization component orthogonal to the pump does not fully thermalize. Hesten *et al* [20] computed a phase diagram depending on a thermalization parameter and pump power, distinguishing regions of Bose-Einstein condensation, multi-mode condensation and lasing.

We will look at the steady state solutions of this model and see how they differ from the equilibrium situation presented in Section 2.3.

Steady state occupations and the condensation threshold

If we fix $f_{\mathbf{m}}$ we can find a steady state solution for $N_{\mathbf{m}}$,

$$N_m = \frac{f_{\mathbf{m}}\Gamma_{\downarrow}^{(\mathbf{m})}}{\kappa/\rho_0 + \Gamma_{\uparrow}^{(\mathbf{m})} - f_{\mathbf{m}}(\Gamma_{\downarrow}^{(\mathbf{m})} + \Gamma_{\uparrow}^{(\mathbf{m})})}. \tag{4.5}$$

It is convenient to define a thermalization coefficient $\theta_{\mathbf{m}}$, which is a measure of how likely it is that a photon exits the cavity before being reabsorbed.

$$\theta_{\mathbf{m}} = \frac{\kappa}{\rho_0 \Gamma_{\uparrow}^{(\mathbf{m})}}. \tag{4.6}$$

This is the inverse of the thermalization coefficient defined in [20]. We have chosen this definition to simplify notation. When $\theta_{\mathbf{m}} \ll 1$ reabsorption is very likely, and we would expect the photon gas to thermalize to the dye. We can use this thermalization coefficient and the Kennard-Stepanov relation $\Gamma_{\uparrow}^{(\mathbf{m})} = \Gamma_{\downarrow}^{(\mathbf{m})} e^{\beta\hbar\delta_{\mathbf{m}}}$ to rewrite Eq. 4.5 as

$$N_{\mathbf{m}} = \frac{1}{e^{\beta\hbar\delta_{\mathbf{m}}}\left(\frac{\theta_{\mathbf{m}}+1}{f_{\mathbf{m}}} - 1\right) - 1} \approx \frac{1}{e^{\beta(\hbar\omega_{\mathbf{m}} - \mu_{\mathbf{m}})}(\theta_{\mathbf{m}} + 1) - 1}, \tag{4.7}$$

where we introduce the effective chemical potential for mode $\mathbf{m}$

$$\mu_{\mathbf{m}} = \hbar\omega_{\text{ZPL}} + k_B T \log f_{\mathbf{m}}, \tag{4.8}$$

which can be interpreted as the local chemical potential of the dye excitations across the mode $\mathbf{m}$. Thus, when $\theta_{\mathbf{m}} <\!\!\ll 1$ the cavity modes are in equilibrium with the dye. If in addition to this, $f(\mathbf{r})$ is approximately constant over several oscillator lengths Eq. 4.7 reduces to the Bose-Einstein distribution and the photon gas will behave as described in

Section 2.3. Otherwise the chemical potential at which the ground state condenses shifts to $\mu_{\mathbf{0}}^{\text{crit}} = \hbar\omega_{\mathbf{0}} + k_B T \log(\theta_{\mathbf{0}} + 1)$, which corresponds to a critical excitation density of

$$f_{\mathbf{0}}^{\text{crit}} \approx e^{\beta(\mu_{\mathbf{0}}^{\text{crit}} - \hbar\omega_{\text{ZPL}})} = e^{\beta\delta_{\mathbf{0}}}(\theta_{\mathbf{0}} + 1) \tag{4.9}$$

Because the thermalization coefficient of the ground state $\theta_{\mathbf{0}}$ is inversely proportional to the absorption rate, thermalization will improve when the cutoff frequency is increased. The dependence of the thermalization parameter on wavelength is plotted in Fig. 4.1a.

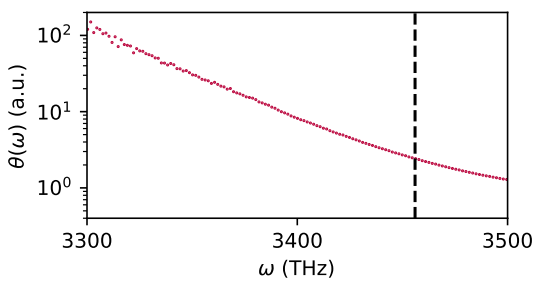

(a) Thermalization coefficient versus frequency for a fixed loss rate κ. The dashed line marks the zero-phonon line. Plotted with spectral data from [12].

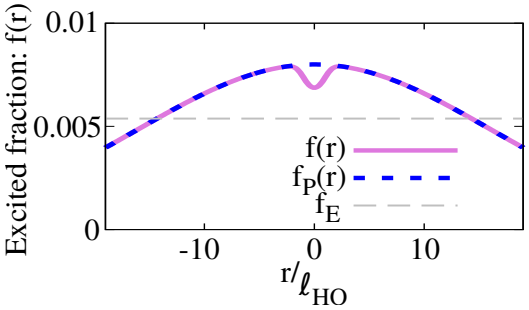

(b) Graph from [18] showing gain clamping in the excitation density in simulation results.

The steady state excitation profile and gain clamping

The steady state solution of Eq. 4.2 is

$$f(\mathbf{r}) = \frac{\Gamma_{\uparrow}^{\text{tot}}(\{N_{\mathbf{m}}\}, \mathbf{r})}{\Gamma_{\uparrow}^{\text{tot}}(\{N_{\mathbf{m}}\}, \mathbf{r}) + \Gamma_{\downarrow}^{\text{tot}}(\{N_{\mathbf{m}}\}, \mathbf{r})}. \tag{4.10}$$

At low densities and/or large cutoff wavelengths the contribution of the cavity modes to the emission and absorption rates can be neglected. The excitation density can then be approximated by

$$f(\mathbf{r}) \approx \frac{\Gamma_{\uparrow}(\mathbf{r})}{\Gamma_{\uparrow}(\mathbf{r}) + \Gamma_{\downarrow}} \approx \frac{\Gamma_{\uparrow}(\mathbf{r})}{\Gamma_{\downarrow}}. \tag{4.11}$$

This condition is met for high energy modes, which will have an occupation of

$$N_{\mathbf{m}} = e^{-\beta\hbar\delta_{\mathbf{m}}} \frac{f_{\mathbf{m}}}{\theta_{\mathbf{m}} + 1} = \frac{1}{\Gamma_{\downarrow}} \frac{e^{-\beta\hbar\delta_{\mathbf{m}}}}{\theta_{\mathbf{m}} + 1} \int d^2\mathbf{r} |\psi_{\mathbf{m}}(\mathbf{r})|^2 \Gamma_{\uparrow}(\mathbf{r}), \tag{4.12}$$

Thus the occupation of high energy modes depends on three things: the temperature T, the pump $\Gamma_{\uparrow}(\mathbf{r})$ and the thermalization coefficient $\theta_{\mathbf{m}}$. For atomic condensates it is customary to determine the temperature by fitting to the thermal cloud. Eq. 4.12 shows that this method is not reliable unless the thermalization coefficient is very small and the excitation density is uniform over the area where the temperature is fitted. The thermal cloud will shrink as the pump spot is made smaller, thus making it look like the thermal cloud is becoming colder. This explains why fits to experimental data tend to find temperatures far below room temperature [21].

Above threshold the contribution of condensed modes can be significant. Suppose the ground state has condensed and dominates emission and absorption. Then the excitation density in the center of the cavity can be approximated by

$$f(\mathbf{0}) \approx \frac{|\psi_{\mathbf{0}}(\mathbf{0})|^2 \Gamma^{\mathbf{0}}_{\uparrow} N_{\mathbf{0}}}{|\psi_{\mathbf{0}}(\mathbf{0})|^2 (\Gamma^{\mathbf{0}}_{\uparrow} + \Gamma^{\mathbf{0}}_{\downarrow}) N_{\mathbf{0}}} \approx \frac{1}{e^{-\beta \delta_{\mathbf{0}}} + 1}, \tag{4.13}$$

where we again made use of the Kennard-Stepanov relation. The chemical potential of the dye excitations thus locks to the energy of the ground state $\hbar\omega_{\mathbf{0}}$. This is also known as gain clamping in laser physics. The result is a dip in the excitation profile, as can be seen in Fig. 4.1b. The purple line is the excitation density, the blue dashed line is the excitation density without emission to and absorption from the cavity modes (Eq. 4.11) and the grey dashed line is the excitation density at maximal gain clamping (Eq. 4.13). Increasing the total pump rate further will push the fringes of the dip up through the critical excitation density of the modes located on the fringes. These modes will then also condense. Fig. 4.2 shows such multimode condensation. The effect of gain clamping becomes more pronounced when the cutoff frequency is increased, because the absorption and emission rates are larger. But as we saw before, thermalization is better for larger cutoff frequencies. As κ/ρ_0 is limited by the quality of the mirrors and by quenching at high concentrations fixed, one has find a balance between good thermalization and single mode condensation.

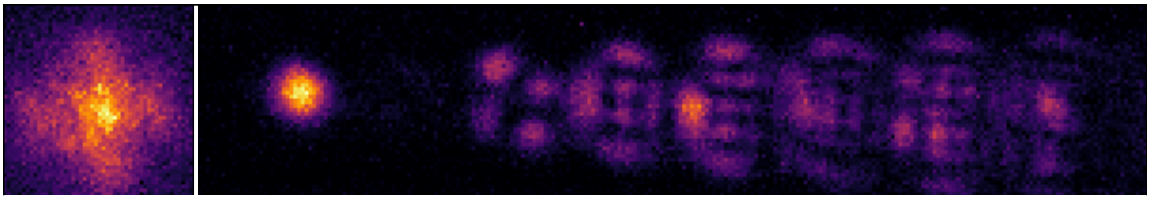

Figure 4.2: Example of multimode condensation, the photon distribution is shown on the left, and the corresponding spectrum on the right.

4.2.1 Imperfections of the dye

There are a properties of the Rhodamine 6G dye which one should keep in mind when doing experiments. First there is photoblinking. This is the decay of excited dye molecules to an excited triplet state for which decay to the ground state singlet is forbidden. The dye molecule can then no longer fluoresce until it returns to the excited state singlet via thermal activation. The typical timescale for this process is around 4 µs [22]. As the integration time of our camera is 200 µs, emission from molecules that have been in the triplet state could affect our measurements. The magnitude of this signal is however very small due to the slow rate of decay to the triplet state.

The second effect is photobleaching, which is an irreversible modification of the molecule mediated by photon absorption. Bleaching slowly reduces the density of the dye ρ_0 after many pulses.

The third effect is that at high concentrations, self-quenching can lead to dissipation rather than emission. The close proximity between dye molecules allows the formation of queching complexes which have fast radiationless decay channels. For Rhodamine 6G in methanol, the concentration at which quenching processes become relevant was found to be about 5 mM [23]. These radiationless decays decrease the quantum yield, the ratio between the number of emitted and absorbed photons, which in the absence of quenching is typically 0.95 [24].

4.3 Experiments

We have performed a number of experiments to look at the behavior around threshold and at multimode condensation. To look at the influence of the dye concentration and cutoff wavelength separately, we perform four experiments: 1.5 mM at 590 nm, 1.5 mM at 576 nm, 6.0 mM at 593 nm and 6.0 mM at 576 nm. These wavelengths were chosen to be within a few nanometers of the efficiency maxima of our echelle grating. At dye concentration 1.5 mM there was not enough laser power available to condense at wavelengths above 590 nm.

Each experiment consists of 200 runs of 100 frames. The cavity is aligned to minimize multimode condensation, keeping the condensation single mode for the majority of the pump power range. During each run, the pump power is scanned across threshold using an interleaved power ramp. The ground state is fitted using the procedure detailed in Section 3.2.1. The data points are sorted by the total number of counts in the image coming from the large mirror and are binned into 100 equally sized bins. The image of the large mirror and the spectrum are averaged across each bin. We use the averaged large mirror images to compute the total number of counts and average radial profiles of the photon distribution. We fit the number of counts in each of the energy levels to the averaged spectra. As the light is split unevenly across the two images (see Fig. 3.1), we correct for this by dividing by the fraction of light being used to make each image. When we refer to 'counts' below, it thus means the following: the number of photons that leaves the cavity through the large mirror multiplied by their detection efficiency.

4.3.1 Cutoff wavelength 590 nm, 1.5 mM

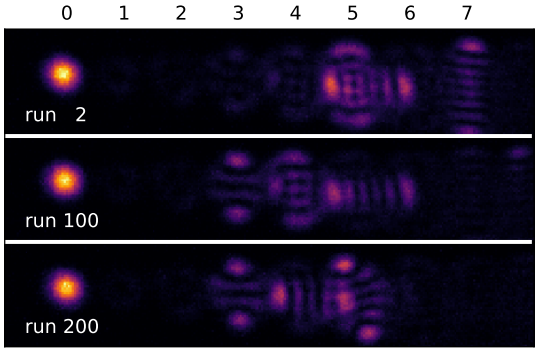

(a) Images of the spectrum at maximal pump intensity.

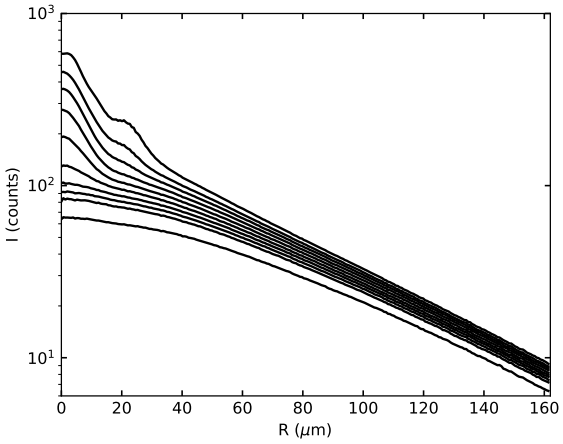

(b) Average radial profiles for rising total counts.

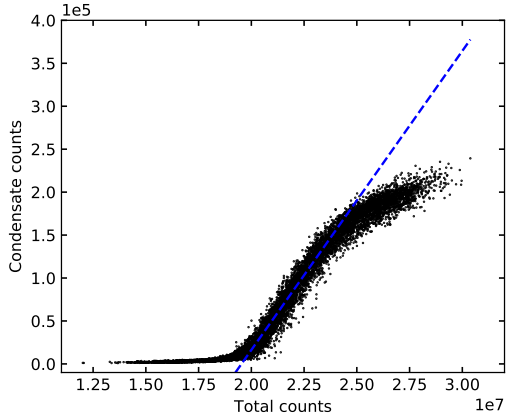

(c) Condensate counts as a function of total counts.

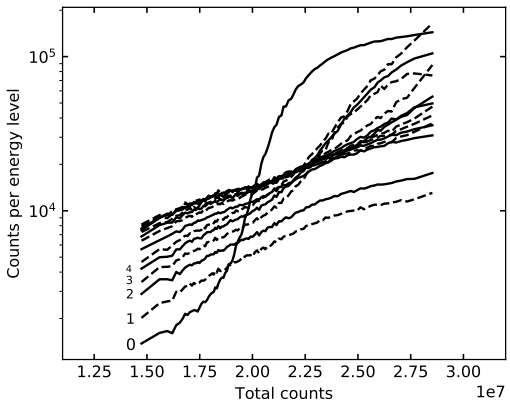

(d) Counts per energy level as a function of total counts. The first five energy levels are labeled.

Figure 4.3: Condensation at cutoff wavelength 590 nm, dye concentration 1.5 mM, dataset **2018-05-09a**

Fig. 4.3 shows the analysis for the experiment at a dye concentration of 1.5 mM and a cutoff wavelength of 590 nm. Fig. 4.3a shows images of the spectrum at maximal pump intensity from the start, middle and end of the experiment. The condensation of higher order modes is clearly visible. Many modes, such as the $(m_x, m_y) = (0, 7)$ mode, can be easily identified. In the top image one can see the anisotropy displayed in the fact that the $(m_x, m_y) = (5, 0)$ and $(m_x, m_y) = (0, 5)$ modes are not aligned. The change in which modes condense is likely due to slow drift of the alignment during the experiment. Fig. 4.3b shows averaged radial profiles for increasing total counts. Condensation is visible in the center of the trap. At first only the ground state condenses, but afterwards a bump at roughly 20 µm appears. Note that the intensity far from the center continues to grow after threshold, meaning that the excited states are not saturated. Fig. 4.3c shows the number of counts from the ground state as a function of the total number of counts. Just above threshold the relationship between the two is linear. The coefficient of this line is the product between the efficiency of the spectral imaging path and $dN_\mathbf{0}/dN_{tot}$. For a thermalized system, we would expect that this $dN_\mathbf{0}/dN_{tot} = 1$ (see Eq. 2.16). However, the coefficient is 0.035, roughly a factor of 20 smaller than the estimated spectral imaging path efficiency, which is around 0.7. This is another sign that the excited states do not become saturated. Fig. 4.3d shows the occupations of the first 14 energy levels. Multimode condensation is visible in the third, fourth and fifth energy levels. The second and third energy levels show no condensation, but they also do not show the crossing at zero chemical potential or saturation above threshold that would occur at good thermalization.

4.3.2 Cutoff wavelength 576 nm, 1.5 mM

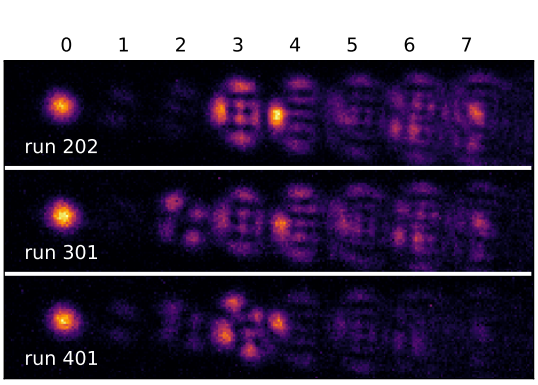

(a) Images of the spectrum at maximal pump intensity.

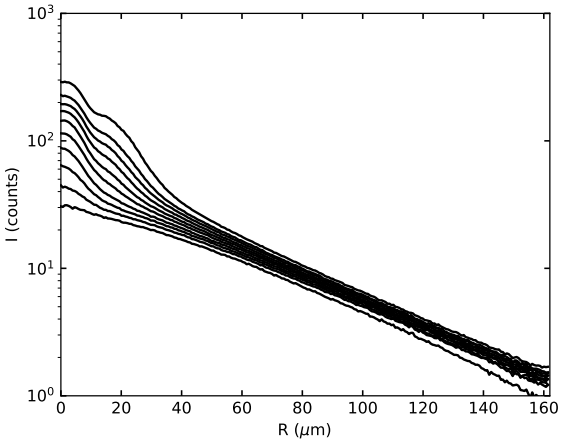

(b) Average radial profiles for rising total counts.

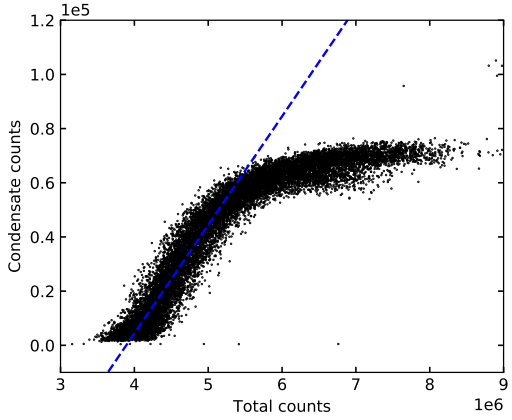

(c) Condensation occupation as a function of total counts

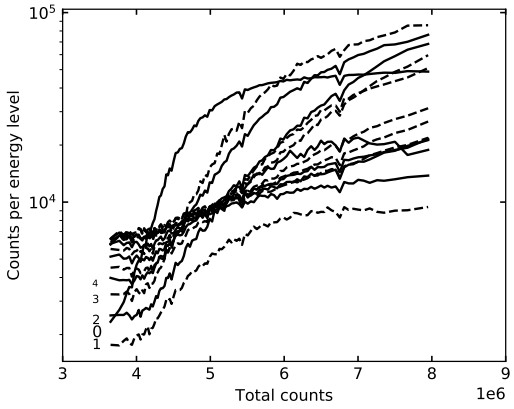

(d) Counts per energy level as a function of total counts. The first five energy levels are labeled.

Figure 4.4: Condensation at cutoff wavelength 576 nm, dye concentration 1.5 mM, dataset **2018-05-24b**

Fig. 4.4 shows the analysis for the experiment at a dye concentration of 1.5 mM and a cutoff wavelength of 576 nm. Fig. 4.4a shows the multimode condensation occurring at maximal pump intensity. Fig. 4.4b shows the averaged radial profiles for increasing total counts. Multimode condensation occurs rather quickly, and is more significant than for cutoff wavelength 590 nm. Again the intensity far from the center of the cavity is not saturated above threshold. Fig. 4.4c shows the occupation of the ground state as a function of the total number of counts. The deviation from the initial linear relationship occurs rather quickly. Fig. 4.4d shows the occupations of the first 14 energy levels. The point where the occupation of the ground state crosses that of the first excited states is unfortunately just outside the range of the experiment. Multimode condensation can be seen to set in quickly, with some energy levels surpassing the ground state in counts. The second and third energy level occupations seem to level off far above threshold, but it is unclear whether this can be considered saturation or a consequence of gain clamping caused by overlapping condensed modes.

4.3.3 Cutoff wavelength 593 nm, 6.0 mM

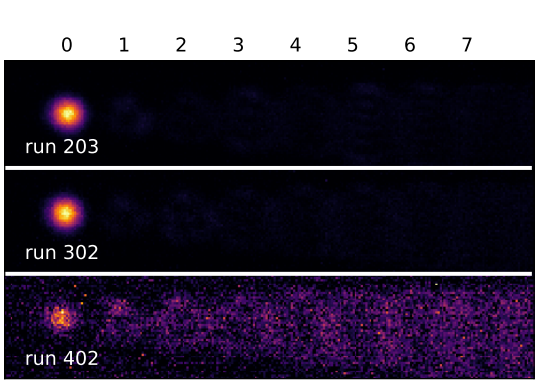

(a) Images of the spectrum at maximal pump intensity.

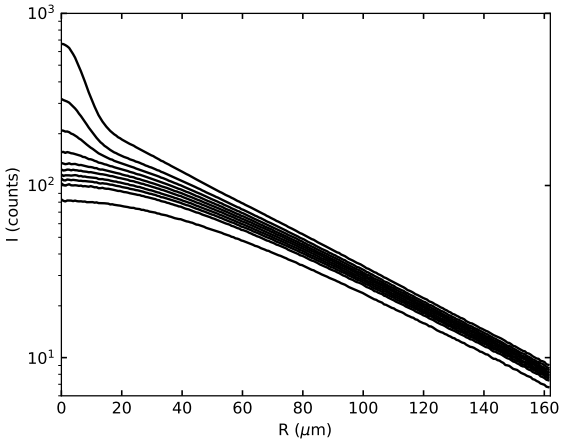

(b) Average radial profiles for rising total counts.

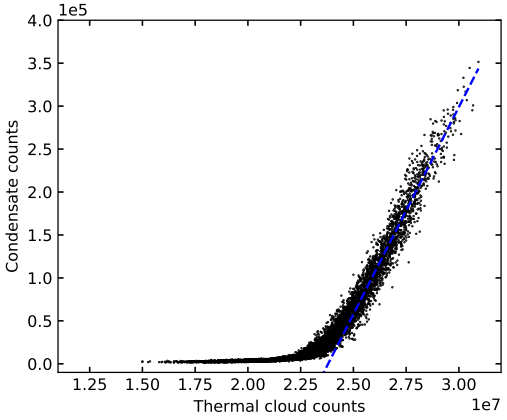

(c) Condensation occupation as a function of total counts

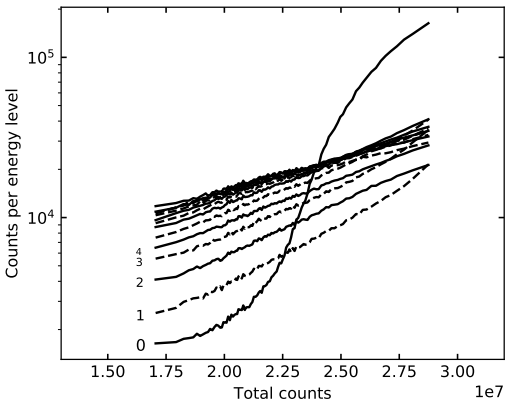

(d) Counts per energy level as a function of total counts. The first five energy levels are labeled.

Figure 4.5: Condensation at cutoff wavelength 593 nm, dye concentration 6.0 mM, dataset **2018-05-25b**

Fig. 4.5 shows the analysis for the experiment at a dye concentration of 6 mM and a cutoff wavelength of 593 nm. Fig. 4.5a shows the spectrum at maximal pump intensity. No clear multimode condensation is visible. During the experiment the absorbed pump power decreases because the dye bleaches faster than for a concentration of 1.5 mM. The result is that the chemical potential associated with a certain pump power decreases over time. The third image is only just above threshold. Fig. 4.5b shows the averaged radial profiles for increasing total counts. Again the intensity far from the center of the cavity is not saturated above threshold, but the growth is slower than at the lower concentration. Fig. 4.5c shows the occupation of the ground state as a function of the total number of counts. No deviation from the linear relationship to the total number of counts can be seen, but the coefficient is still small, so again we see that no saturation has occurred. The critical number of photons is larger than in Fig. 4.3c. Fig. 4.5d shows the occupations of the first 14 energy levels. No multimode condensation can be seen, but at high pump powers some of the excited states start to cross.

4.3.4 6.0 mM 576 nm

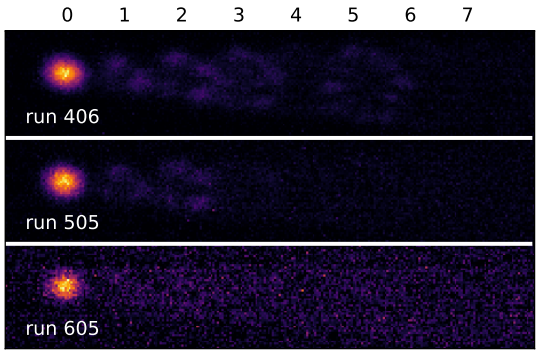

(a) Images of the spectrum at maximal pump intensity.

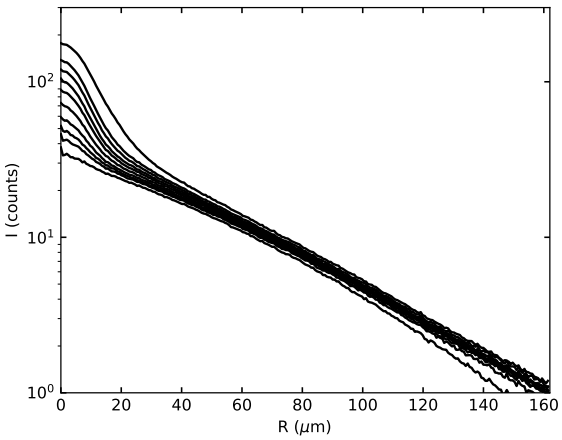

(b) Average radial profiles for rising total counts.

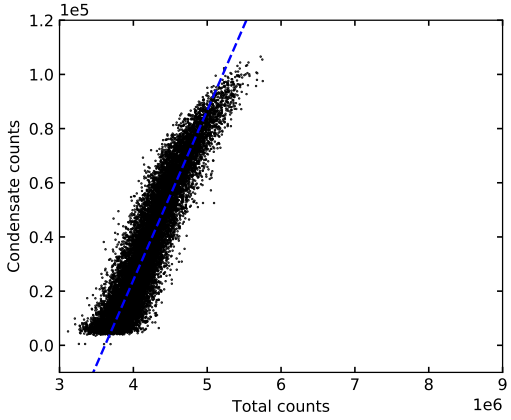

(c) Condensation occupation as a function of total counts. The range of the x axis is the same as Fig. 4.4c for easy comparison.

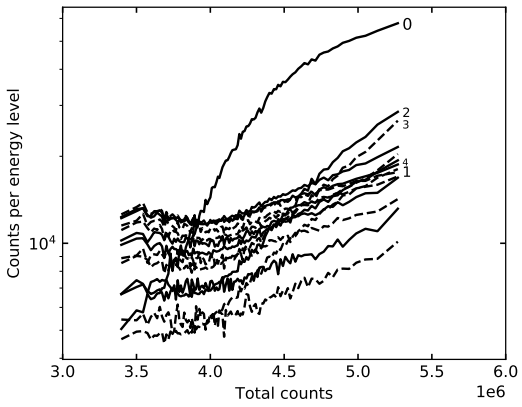

(d) Counts per energy level as a function of total counts. The first five energy levels are labeled.

Figure 4.6: Condensation at cutoff wavelength 576 nm, dye concentration 6.0 mM, dataset **2018-05-25c**

Fig. 4.6 shows the analysis for the experiment at a dye concentration of 6 mM and a cutoff wavelength of 576 nm. Fig. 4.6a shows the spectrum at maximal pump intensity. Weak multimode condensation can be seen in the second, third and fourth energy levels, and the effect of dye bleaching is again visible. Fig. 4.6b shows the averaged radial profiles for increasing total counts. There is no clear sign of multimode condensation until the widening of the peak at high total counts. Again the intensity far from the center of the cavity is not saturated above threshold, but the growth is slightly slower than at the lower concentration. Fig. 4.6c shows the occupation of the ground state as a function of the total number of counts. Compared to the data for 1.5 mM in 4.4c, multimode condensation occurs at higher condensate counts and the slope has increased. Fig. 4.6d shows the occupations of the first 14 energy levels. The averaged spectra contain a background signal, which has led to bad fits at low intensities. At high intensities some multimode condensation can be seen, and there is again no saturation of the excited states.

4.4 Conclusion and Discussion

Our results show that with current experiment parameters, the photon gas cannot be considered to be in thermal equilibrium. This is evident in the fact that the thermal cloud does not saturate above threshold, and that none of the experiments showed a point where all low energy levels were equally occupied.

The observations of the effects of wavelength on multimode condensation agree qualitatively with the predictions of the rate equation model. A shorter cutoff wavelength leads to more significant gain clamping, which causes multimode condensation. We also observe that a higher dye concentration affects multimode condensation. This is not immediately apparent from Eq. 4.10, as the dye density does not appear in it. A possible explanation lies in the quenching that occurs at higher concentrations (see Section 4.2.1). This increases the non-cavity decay rate $\Gamma_{\downarrow}$, and the pump rate $\Gamma_{\uparrow}(\mathbf{r})$ must thus also be increased to still reach condensation. Spontaneous emission and absorption are thus a smaller fraction of the total decay and excitation of dye molecules respectively.

When looking at the images of multimode condensation at 1.5 mM, Fig. 4.3a and Fig. 4.4a, one notices that no condensation occurs for the modes in the $m = 1$ and $m = 2$ levels. This seems to contradict the explanation of gain clamping in Section 4.2, which would result in condensation starting at the center of the trap and moving outward, condensing lower energy modes first. This discrepancy may be a result of our experimental procedure. As explained at the start of Section 4.3, before the experiments the cavity mirrors were aligned to minimize multimode condensation. There must therefore be something in the alignment of the mirrors that affects the condensation threshold (Eq. 4.9) of the modes by changing their thermalization coefficient. The alignment procedure shifts the mirrors a few hundred micrometers at the most, while the curvature of the mirrors is 1 m. The alignment thus does not have a large effect on the trap frequency, so the absorption rate is unaffected. This is thus not the origin of the change in thermalization coefficients. Another possibility is that the reflectivity of the mirrors is inhomogeneous, and that the alignment procedure leads to a cavity where the center of the trap is a local reflectivity maximum. This would lead to a local minimum for the loss rate κ and a thermalization coefficient for the ground state that is lower than that for the states in the $m = 1$ and $m = 2$ levels. The critical excitation density, Eq. 4.9 for these modes is increased, and they will not condense. Once multimode condensation starts for modes with $m > 2$, gain clamping from these higher order modes maintains the excitation density below the critical point for the $m = 1$ and $m = 2$ modes.

The hypothesis that the inhomogeneity of the mirrors has a significant effect on which modes can condense is supported by the observation (as for example in Fig. 4.4a) that not all modes in an energy level condense. The ones that do condense can change over time as the alignment drifts.

Further study into the rate equation model and how we can relate its predictions to the experiment could yield valuable diagnostic methods. For example, if we are able to increase the size of the pump spot significantly such that the excitation density is flat over several oscillator lengths and measure the spectrum far below threshold, Eq. 4.7 reduces to a Boltzmann factor divided by $\theta_{\mathbf{m}} + 1$, giving us a way to measure the thermalization parameters. Because this measurement is far below threshold, pump powers can be kept low. Because of the low occupations of the modes, we either have to increase the pulse duration or sum the images over multiple pulses. In both cases the stability of the cavity length is the limiting factor. If the cavity length changes too much the image is blurred and we can no longer distinguish the energy levels.

5 Effective photon-photon interactions

5.1 Introduction

The strong interparticle interactions in, for example, polariton condensates, allow for the study of interesting physics, notably superfluid behavior such as quantized vortices [25]. A connection can even be made to gravitational physics by creating a black hole analogue for sound waves in the condensate, which has been done in atomic BECs [26]. A section of the paper reporting the first photon condensate by Klaers *et al* [8] showed that the condensate appeared to grow in size with increasing condensate fraction (see Fig. 5.1a), which suggested that there were significant repulsive interactions between the photons. Previous work in our group [27] observed condensate growth similar to that of Klaers *et al*. These results can be seen in Fig. 5.1b. The possibility of multimode condensation being the origin of the observed growth has made these results difficult to interpret without doing additional experiments, as their determination of the condensate size depends on the assumption of thermal equilibrium and single mode condensation. To get around this difficulty, we can use the current setup to image the ground state directly.

We will first look at some theory about the two kinds of interactions that we would expect. Then we will apply the old and new analysis methods to experimental data and compare the results. Finally we will examine the changes that occur at different wavelengths and dye concentrations.

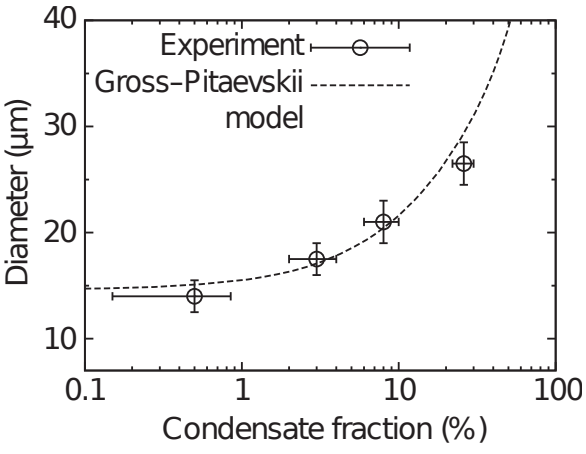

(a) Observations of condensate growth by Klaers *et al* [8]

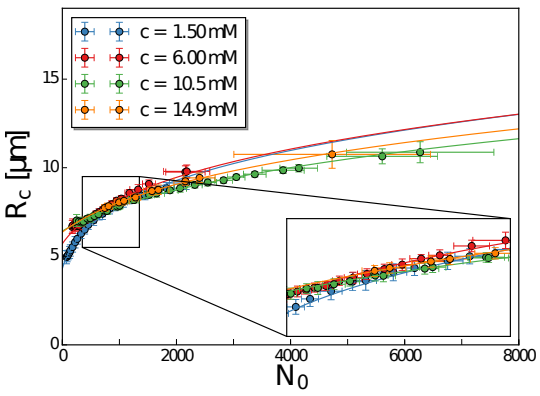

(b) Observations of condensate growth in our group [27]

5.2 Theory

Optical nonlinearities occur when the refractive index of a material depends on the intensity of the light passing through it. To see how these nonlinearities will look when put into our effective harmonic oscillator Hamiltonian, we need to go back to the expression for the energy of the photon

$$E_{ph}(\mathbf{r}) \approx m_{ph}\left(\frac{c}{n}\right)^2 + \frac{(\hbar\mathbf{k}_\perp)^2}{2m_{ph}} + \frac{1}{2}m_{ph}\Omega^2\mathbf{r}^2. \tag{5.1}$$

When the refractive index changes, it results in a change to the rest energy belonging to the longitudinal part of the wave

$$\Delta E_{ph} = -m_{ph}\left(\frac{c}{n_0}\right)^2\frac{\Delta n}{n_0}. \tag{5.2}$$

If this change in refractive index is dependent on position, it can be seen as an additional effective potential. If it is also dependent on the photon density, it can be considered a nonlinearity. We can separate the change in refractive index into two parts having different physical origins. The first is an instantaneous Kerr effect. The second is a slow response due to heating of the solvent by dissipation.

5.2.1 Instanteous interactions

The simplest of these nonlinearities is the Kerr effect, a dependence of the refractive index on the intensity of light $\Delta n_{\text{Kerr}}(\mathbf{r}) = n_2 I(\mathbf{r})$. We can model this as an instantaneous contact interaction with an interaction strength we denote by g. The Hamiltonian is then

$$H = \int d^2\mathbf{r}\Big[-\hat{\psi}^\dagger(\mathbf{r})\frac{\hbar^2}{2m}\nabla^2\hat{\psi}(\mathbf{r}) + \frac{1}{2}m_{ph}\Omega^2\mathbf{r}^2\hat{\psi}^\dagger(\mathbf{r})\hat{\psi}(\mathbf{r}) + \frac{g}{2}\hat{\psi}^\dagger(\mathbf{r})\hat{\psi}^\dagger(\mathbf{r})\hat{\psi}(\mathbf{r})\hat{\psi}(\mathbf{r})\Big] \tag{5.3}$$

To simplify notation, we can make this dimensionless by expressing distances in units of the harmonic oscillator length l_{HO} and energies in terms of $\hbar\Omega$ and rewrite the Hamiltonian as

$$H = \frac{1}{2}\int d^2\mathbf{r}\Big[\hat{\psi}^\dagger(\mathbf{r})\Big(-\nabla^2 + \mathbf{r}^2\Big)\hat{\psi}(\mathbf{x}) + \tilde{g}\hat{\psi}^\dagger(\mathbf{r})\hat{\psi}^\dagger(\mathbf{r})\hat{\psi}(\mathbf{xr})\hat{\psi}(\mathbf{r})\Big]. \tag{5.4}$$

Here $\tilde{g} = mg/\hbar^2$ is known as the dimensionless interaction strength. The field can be decomposed into harmonic oscillator eigenstates

$$\hat{\psi}(\mathbf{r}) = \sum_{\mathbf{m}}\psi_{\mathbf{m}}(\mathbf{r})\hat{a}_{\mathbf{m}}. \tag{5.5}$$

Which leads to the following equation for the ground state wavefunction $\psi_{\mathbf{0}}(\mathbf{r})$ in the Hartree-Fock approximation [28]

$$\Big\{-\nabla^2 + \mathbf{r}^2 + \tilde{g}[n_{\mathbf{0}}(\mathbf{r}) + 2n_{ex}(\mathbf{r})]\Big\}\psi_0(\mathbf{r}) = \epsilon_{\mathbf{0}}\psi_{\mathbf{0}}(\mathbf{r}) \tag{5.6}$$

where the density of condensate photons is $n_{\mathbf{0}}(\mathbf{r}) = \langle\hat{a}_{\mathbf{0}}^\dagger\hat{a}_{\mathbf{0}}\rangle|\psi_{\mathbf{0}}(\mathbf{r})|^2$ and the density of photons in the excited states is $n_{ex}(\mathbf{r}) = \sum_{\mathbf{m}\neq 0}|\psi_{\mathbf{m}}(\mathbf{r})|^2\langle\hat{a}_{\mathbf{m}}^\dagger\hat{a}_{\mathbf{m}}\rangle$. The condensate thus feels an additional effective potential of the form

$$V_{Kerr}(\mathbf{r}) \propto \tilde{g}[n_{\mathbf{0}}(\mathbf{r}) + 2n_{ex}(\mathbf{r})]. \tag{5.7}$$

For $\tilde{g} > 0$, the interactions are repulsive, and the condensate will grow in size when the occupation increases. Previously reported values of $\tilde{g}$ have been $\tilde{g} \sim 7\times10^{-4}$ [8] and $\tilde{g} \sim 10\times10^{-2}$ [27].

5.2.2 Thermal lensing

The second kind of nonlinear effect is a change in the refractive index due to heating, known as thermal lensing. This can be modeled using a field ΔT, the local temperature modification as in [29]. The equations for the temperature field ΔT and the ground state wavefunction $\psi_{\mathbf{0}}$ are then

$$\frac{\partial \Delta T(\mathbf{r},t)}{\partial t} = \frac{K}{C_v}\nabla^2 \Delta T(\mathbf{r},t) + S(\mathbf{r},t) \tag{5.8}$$

$$i\hbar \frac{\partial \psi_{\mathbf{0}}(\mathbf{r},t)}{\partial t} = \left\{ -\frac{\hbar^2}{2m_{ph}}\nabla^2 + \frac{1}{2}m_{ph}\Omega^2\mathbf{r}^2 - m_{ph}\left(\frac{c}{n_0}\right)^2 \frac{\eta \Delta T(\mathbf{r},t)}{n_0} \right\} \psi_{\mathbf{0}}(\mathbf{x}), \tag{5.9}$$

where $S(\mathbf{r},t)$ is some heat source, and K, C_v and $\eta = \partial n/\partial T$ are the thermal conductivity, volume heat capacity and thermo-optic coefficient of ethylene glycol respectively. As η is negative, a temperature maximum in the center of the cavity will reduce the curvature of the trap.

Theoretical work on interactions through thermal lensing has used the condensate intensity as a source term [29]. We will here instead apply the rate equation model presented in chapter 4 to .

Heat diffusion is a slow process, which can be neglected for 500 ns pulses. We can thus approximate that the effective potential from thermal lensing is

$$V_{Th}(\mathbf{r},t) \propto \int dt S(\mathbf{r},t). \tag{5.10}$$

There are two sources of heat in the cavity. The first source is the energy dissipated by excited dye molecules as they thermalize with the solvent. This source depends only on the pump spot, and not on the occupation of the cavity modes, so it cannot be considered a nonlinearity. It leads to an effective potential of

$$V_{Th,\mathrm{pump}}(\mathbf{r},t) \propto t \times \Gamma_{\uparrow}(\mathbf{r}). \tag{5.11}$$

The second source of heat is non-radiative decays of excited dye molecules. This source is proportional to the excitation density $f(\mathbf{r})$ We thus expect that, assuming steady state conditions for $f(\mathbf{r})$, the effective potential due to nonradiative decays will be

$$V_{Th,\mathrm{dis}}(\mathbf{r},t) \propto t \times \rho_0 f(\mathbf{r}). \tag{5.12}$$

The condensate size will change over time in response to the effective potential. The effects are small and the heating takes place over the course of 500 ns, so the process is expected to be adiabatic. As the source from nonradiative decays depends on the excitation density, it can be affected by the photon density through gain clamping. High intensities will reduce the amount of dissipation. This leads to effective attractive interactions, as the effective potential is stronger where the intensity is lower.

5.2.3 Interpreting experimental results

The intensity of the condensate light on our camera has the form of a Gaussian function with position (x_0, y_0) on the camera chip and widths l_x and, l_y. Because the light passes over a diffraction grating before being imaged, the position of the image along some axis depends on the wavelength of the light. We will take this to be the x-axis. Now suppose that we start our measurement and the wavelength of the light changes. Then the position of the image changes as well. With the camera, we can only measure the image integrated over the duration of the pulse. This means that if the wavelength of the condensate changes, e.g. by heating of the solvent, the image will be smeared out along the x-axis.

We can therefore interpret the widths of the final distribution as follows: the width along the y-axis R_y is the average width of the condensate during the pulse, which tells us about the curvature of the effective potential. The width along the x-axis R_x is a linear combination between the average width of the condensate and the shift of the condensate wavelength, so it tells us about the change over time of the potential at the center of the cavity, i.e. the change in the cutoff wavelength.

5.3 Experiments

5.3.1 Comparison with previous work

We first compare the previous analysis method [27] [13] to the new analysis method. The analysis method used previously consisted of taking the radial profile of the photon distribution and fitting a density distribution to it. This density distribution is based on the assumption that the photon gas is in thermal equilibrium and corrects for the imperfect imaging of the density far from the cavity center due to clipping in the imaging system [21]. The radius of the ground state is left as a fitting parameter, but the excited states are taken to be the harmonic oscillator eigenstates with thermal occupations corresponding to a certain temperature and chemical potential, which are also fit parameters.

The analysis of the spectral data consists of fitting the condensate as described in Section 3.2.1 and sorting the results into bins according to the number of counts in the condensate. For each bin the weighted average of the condensate sizes along the x-axis and the y-axis are computed. These are then plotted against the average number of counts for that bin.

We use a dye concentration of 1.5 mM, which was found to have the largest $\tilde{g}$ in [27]. We lock the cavity to the cutoff wavelength of 590 nm at mode number $q = 8$. The experiment consists of 200 runs. Each run in turn consists of 100 frames, with the pump power being varied in an interleaved power ramp. The interleaved power ramp keeps the total power of two consecutive pulses constant, to minimize the effect of cumulative heating. The range of pump powers is set to also contain images of the photon distribution below threshold, which is necessary for the old analysis method to establish the number of photons.

The results for the two analysis methods can be seen in Fig. 5.2. For the old analysis method the width is plotted as a function of the number of photons in the condensate N_0, which was calibrated using the assumption of thermal equilibrium. As we do cannot make this assumption, we instead plot the width as a function of the total number of condensate counts. The significant interactions found using the old analysis method are not present in the spectral analysis. The harmonic oscillator length expected for the parameters used is also plotted. The old analysis method consistently underestimates the size of the condensate. The spectral analysis barely shows any growth. Note that the condensate size

is significantly larger than the oscillator length, which is probably a consequence of thermal lensing caused by the pump.

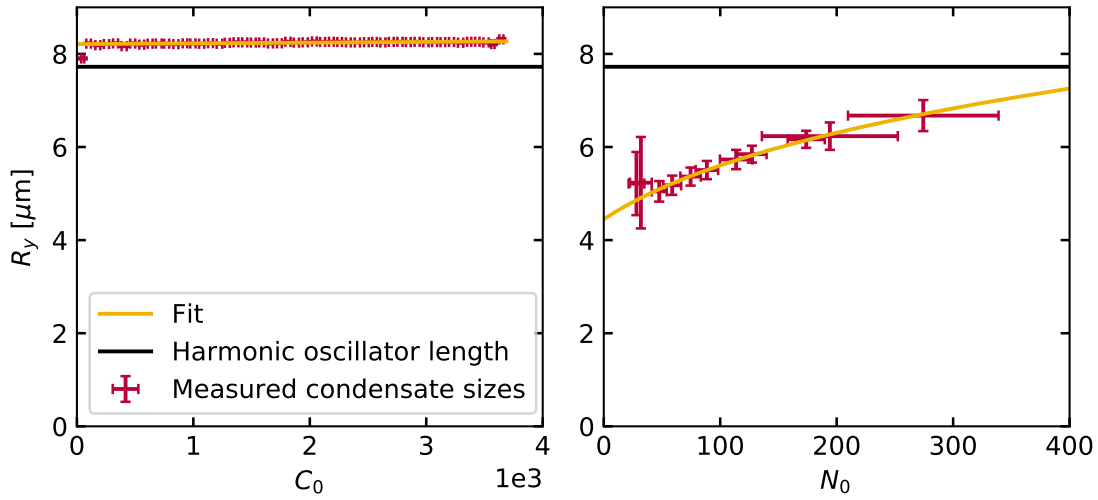

Figure 5.2: Comparison between the new (left) and old (right) analysis methods for dataset **2018-05-09a**.

We can look more closely at the spectral analysis to see that there is in fact some growth occurring. Fig. 5.3 shows the fitted widths along the two axes in micrometers and in harmonic oscillator lengths versus the total number of counts in the condensate C_0. Whilst the condensate size does grow with increasing C_0, we cannot yet conclude that this is due to interaction. This is because the number of condensate counts is necessarily correlated with the total pump power, which in turn is correlated with thermal lensing effects that may be present.

Recall that the expected harmonic oscillator length is smaller along the x-axis due to the anamorphic magnification caused by the grating. The increase with respect to the harmonic oscillator length is much larger along the x-axis, suggesting that slow heating due to dissipation from the pump has shifted the ground state energy during the pump pulse. The graph for the width along the x-axis has an additional feature at low condensate counts. The width decreases at first, and then starts growing again. This could be a sign of gain clamping reducing dissipation.

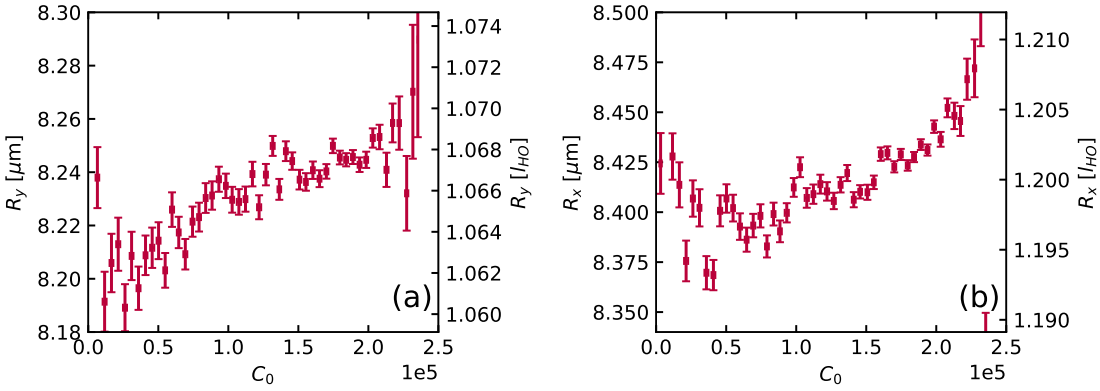

Figure 5.3: Fitted condensate widths for dataset **2018-05-09a**. Condensate widths are expressed in micrometers and in harmonic oscillator lengths.

5.3.2 Increasing dye concentration

The effects of gain clamping can be more clearly seen when the nonradiative decay rate increases. Therefore we increase the dye concentration to 6.0 mM, where quenching decreases the quantum yield. Fig.5.4 shows the fitted widths for this concentration. The width along the x-axis can be seen to vary significantly, confirming that significant heating is taking place. The initial decrease in the width is again present and more pronounced. This supports our hypothesis that the origin of the nonlinearity is the combination of nonradiative decays and gain clamping.

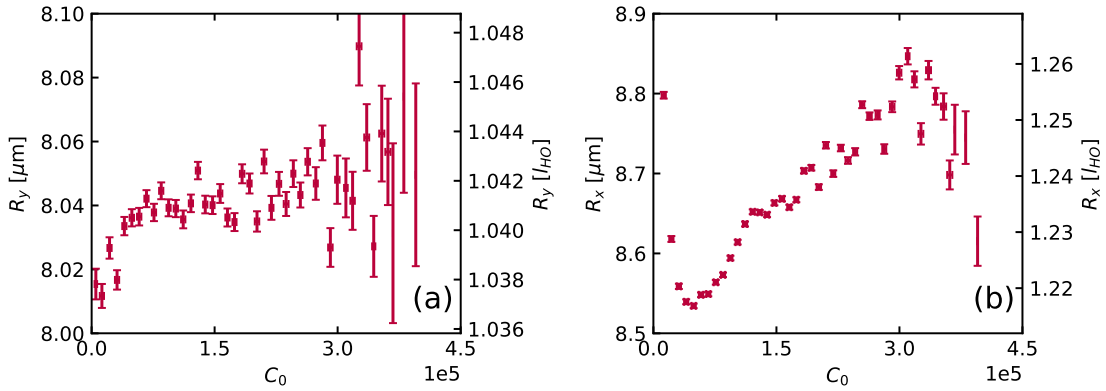

Figure 5.4: Fitted condensate widths for dataset **2018-06-01b**. Condensate widths are expressed in micrometers and in harmonic oscillator lengths.

5.3.3 Varying the cutoff wavelength

By decreasing the cutoff wavelength, we can increase the effect of gain clamping (see Section 4.2). We therefore perform experiments at different cutoff wavelengths. Fig.5.5 shows the results for 1.5 mM. The size of the condensate at 592 nm behaves differently than what we saw at 590 nm in Fig. 5.2. It grows at first, and later shrinks again. The relative flatness of the condensate width and wavelength shift suggest that the thermal lensing due to pump dissipation is roughly constant across the range of pump powers we used. This means that the growth observed at wavelengths 586 nm and 576 nm are due to nonlinearities. In each graph there appears to again be a dip at low condensate counts, with the depth increasing as the cutoff wavelength becomes shorter. At 576 nm the initial downturn is not visible, but this is to be expected because, as we saw in Subsection 4.3.2, the region below threshold is not currently experimentally accessible at this wavelength.

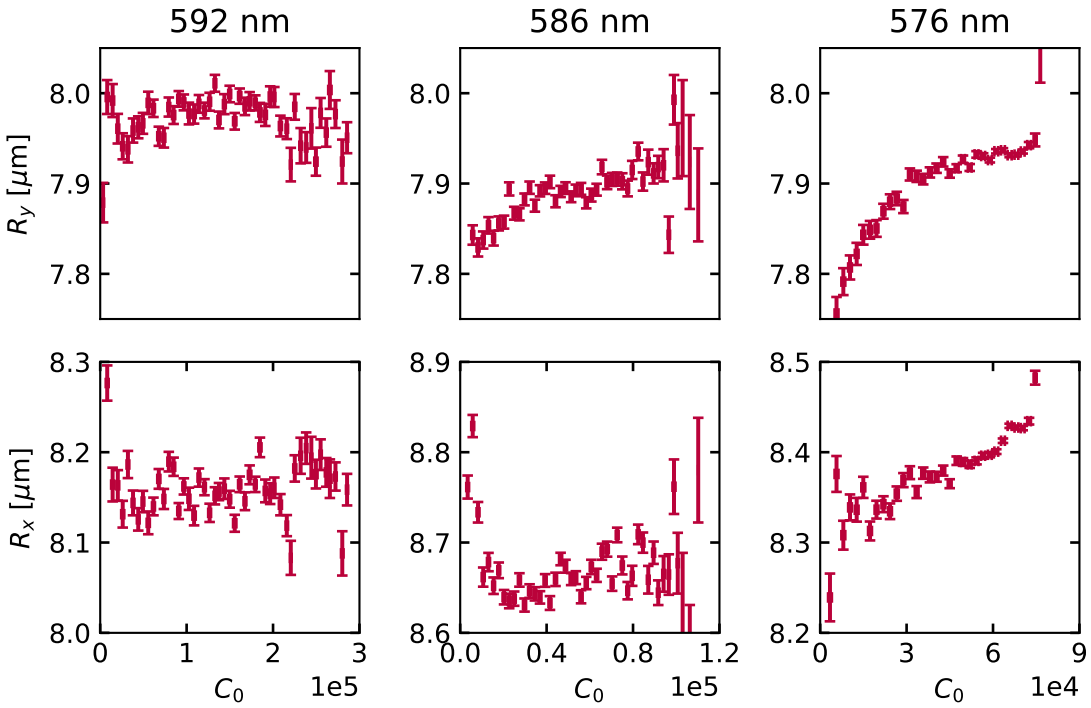

Figure 5.5: Experiments at 1.5 mM. Datasets from left to right: **2018-05-24a**, **2018-05-24c** and **2018-05-24b**

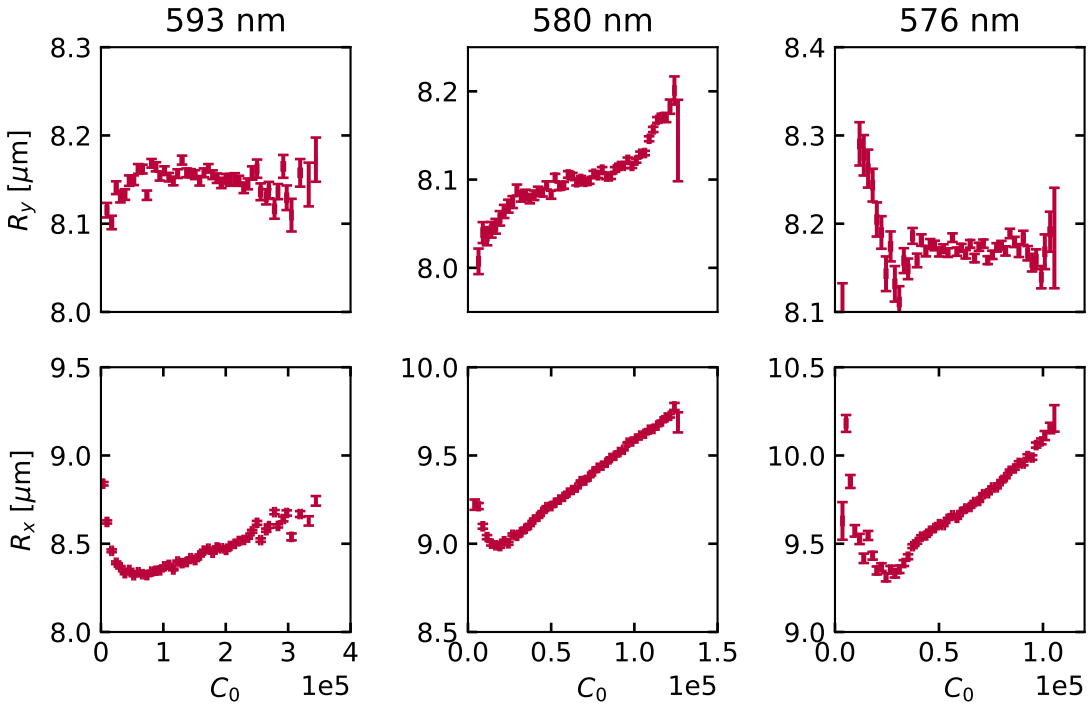

Figure 5.6: Experiments at 6.0 mM. Datasets from left to right: **2018-05-25b**, **dat:2018-05-25d** and **2018-05-25c**

Fig. 5.6 shows the results for a concentration of 6.0 mM. For large wavelength the condensate size behaves the same as for low concentrations, but there is a difference at 576 nm. Something happens at roughly 0.4×10^5 counts. The condensate width becomes constant and there is a kink in wavelength shift. If we look at the mode occupations for this dataset, Fig. 4.6d, we see that this point corresponds with the onset of multimode condensation. With gain clamping occuring not only in the area of the condensate but also around it, the effective potential due to thermal lensing flattens out in the center of the trap and the condensate size remains constant. To see why this happens at a concentration of 6.0 mM but not at 1.5 mM we can look back to the modes that condense for these two cases. Fig. 4.4c shows that at 1.5 mM, the modes in $m = 2$ and $m = 3$ levels do not condense, but in Fig. 4.6c we see that at 6.0 mM they do condense. Therefore, the effective potential at the center of the trap does not flatten out in the results for 1.5 mM because of the lack of gain clamping in the region around the condensate.

5.4 Conclusion and discussion

We can conclude that there are thermal lensing effects in our cavity. The condensate has an effect on this thermal lensing through its interaction with the dye, leading to an effective nonlinearity in the photon field which is time dependent. This nonlinearity is attractive, because high photon densities reduce the dissipation caused by nonradiative decays, which leads to a local minimum in the temperature, and thus a local minimum in the effective potential. No conclusions can yet be drawn about the presence of a Kerr interaction. If it is present the interaction strength is too small to distinguish it from thermal lensing effects.

One feature of the experimental results that is not yet well understood is why the wavelength shifts start increasing again after the initial decrease in Fig. 5.6, as increased condensate occupation should reduce the dissipation even more. A possible explanation for this is that the shift of the ground state energy reduces the condensate occupation during the pulse because the critical excitation density (Eq. 4.9) of the ground state goes up. This leads to a positive feedback loop where a reduction of the condensate occupation increases dissipation, which in turn increases the cutoff wavelength and thus reduces the condensate occupation. If this is the case then there is no steady state solution for the condensate occupation at this concentration. Future experiments on thermalization at high concentrations should keep this in mind.

6
Outlook

Although the rate equation model and our experimental results agree qualitatively, we have limited access to data we can compare quantitatively to theory. There are a number of things that can be done to improve this.

Improved cavity locking

The limited stability of the current cavity locking system makes it difficult to measure the spectrum far below threshold. If the cutoff frequency is stabilized to within the splitting between the levels Ω we have experimental access to the mode occupations far below threshold, where gain clamping can be ignored.

The standard approach for stabilizing a cavity is the Pound-Drever-Hall technique, where a Gaussian laser beam is matched to the one of the Gaussian resonances of the cavity. The laser light is phase modulated to give it two sidebands. The intensity of the light reflected from the cavity can be measured with a fast photodetector to produce a feedback signal that can be used to stabilize the cavity. The drawback of this technique is that it restricts our choices of cutoff wavelengths and mode numbers. We need our cutoff wavelength to be in the range between 570 and 600 nm, and our mode number must be lower than 10 to keep the longitudinal component of our photon gas single mode. If we want to lock the cavity to our HeNe laser, the only options would be to lock the cavity to the $q = 10$ or $q = 11$ resonances of the HeNe laser light, which would give us cutoff wavelengths of 574.5 and 579.3 nm respectively. Ideally an alternative can be found which does not restrict our cavity length to discrete values.

Better pump spot shape and control

The imaging system for the pump spot revealed a significant astigmatism in the pump beam. Fixing this astigmatism would enable us to keep the pump spot roughly circular and change its size. By varying the pump spot size we could study thermal lensing due to pump spot dissipation. A focused spot could be used to condense specific modes by pumping their antinodes.

The anisotropy in the potential observed in Chapter 4 may be the result of thermal lensing with from a noncircular pump spot. If this is the case, we can eliminate this anisotropy by making the pump spot circular. Fitting to the spectrum would then be much easier, as we can take the Laguerre-Gauss modes as our fitting functions.

Further experiments and theory on the thermalization of the photon gas is necessary to esti-

mate the magnitude of the thermalization coefficient in our setup. One option is to measure the threshold pump power as a function of cutoff wavelength and relate the threshold pump power to the critical excitation density Eq. 4.9 through simulations or theory. Over the past few months, our group has written code to numerically solve the rate equations. This could prove useful in improving our understanding of the thermalization process.

Controlling pump pulse length

The current method of chopping the laser beam into pulses uses three AOMs in series. This leads to slow rise and fall times and fluctuations in intensity. To more accurately compare experiment with steady state theory, we want to switch the light on and off in a few nanoseconds, and keep the intensity in between constant. To achieve this we are working on replacing one of the AOMs with a Pockels cell. An additional advantage of the use of a Pockels cell is better control over pulse duration. We can then vary the pulse duration along with the intensity such that the total integrated pulse power is the same over each pulse. The potential coming from pump dissipation (Eq. 5.11) is then constant. Any growth of the condensate size must then be due to nonlinearities.

Appendix A: Glossary

This is a list of the symbols used in this thesis in alphabetical order. Some symbols which appear in only one section are not listed. Numerical values relevant to our experimental setup are given where possible.

Symbol	Defined as	in	Value	Units	Description
β	$(k_B T)^{-1}$	Sec. 2.2	$\sim 2.4 \times 10^{-20}$	J^{-1}	
$D(\mathbf{r})$	$D_0 - 2(R - \sqrt{R^2 - \mathbf{r}^2})$	Eq. 2.3	$\sim 1.7 \times 10^{-6}$	m	distance between the mirrors at position $\mathbf{r}$
$\delta_{\mathbf{m}}$	$\omega_{\mathbf{m}} - \omega_{\mathrm{ZPL}}$	Sec. 4.2	-	Hz	detuning of mode $\mathbf{m}$ from the zero-phonon line
k_z		Sec. 2.1	-	m^{-1}	longitudal wavenumber of the photon gas
$f(\mathbf{r})$		Sec. 4.2	-	1	excitation density
$f_{\mathbf{m}}$	$\int d\mathbf{r} f(\mathbf{r}) \lvert\psi_{\mathbf{m}}(\mathbf{r}\rvert^2$	Sec. 4.2	-	1	overlap between excitation density and mode $\mathbf{m}$
$\tilde{g}$	$mg/\hbar^2$	Sec. 5.2.1	-	1	dimensionless interaction strength
$\Gamma_{\downarrow}$		Sec. 4.2	-	s^{-1}	nonradiative decay rate
$\Gamma_{\downarrow}^{(\mathbf{m})}$		Sec. 4.2	-	$\mathrm{s}^{-1}\mathrm{m}^2$	emission rate to mode $\mathbf{m}$
$\Gamma_{\uparrow}^{(\mathbf{m})}$		Sec. 4.2	-	$\mathrm{s}^{-1}\mathrm{m}^2$	absorption rate of mode $\mathbf{m}$
$\Gamma_{\uparrow}(\mathbf{r})$		Sec. 4.2	-	s^{-1}	pump rate at position $\mathbf{r}$
κ		Sec. 4.2	-	s^{-1}	cavity loss rate
l_{HO}	$\sqrt{\hbar/m_{\mathrm{ph}}\Omega}$	Sec. 2.1	$\sim 7.7 \times 10^{-6}$	m	harmonic oscillator length
λ_c	$\frac{2\pi c}{\omega_c}$	Sec. 3.1.4	590×10^{-9}	m	cutoff wavelength
m_{ph}	$\hbar k_z(0)/c$	Eq. 2.5	$\sim 7.7 \times 10^{-36}$	kg	effective photon mass
μ		Sec. 2.3	-	J	chemical potential
$\mu_{\mathbf{m}}$	$\hbar\omega_{\mathrm{ZPL}} + k_B T \log f_{\mathbf{m}}$	Eq. 4.8		J	effective chemical potential of mode $\mathbf{m}$
n_0		Sec. 2.1	1.43	1	refractive index of ethylene glycol at room temperature
$N_{\mathbf{m}}$				1	occupation of mode $\mathbf{m}$
Ω		Eq. 2.6	$\sim 2.3 \times 10^{11}$	Hz	effective harmonic trap frequency
ω_c		Sec. 2.1	-	Hz	cutoff frequency
ω_{ZPL}		Sec. 2.2	3.456×10^{15}	Hz	zero phonon line of rhodamine 6G
q		Sec. 2.1	8	1	longitudinal mode number of the photon gas
R		Sec. 2.1	1	m	radius of curvature of the mirrors
ρ_0		Sec. 4.2	$1 - 6 \times 10^{18}$	m^{-2}	number density of dye molecules
$\theta_{\mathbf{m}}$	$\kappa/\rho_0\Gamma_{\uparrow}^{(\mathbf{m})}$	Eq. 4.6		1	thermalization coefficient of mode $\mathbf{m}$

Appendix B: Datasets

The fit parameters we use to filter are:

- the position along the x axis x_0, which corresponds to cutoff wavelength,
- the position along the y axis y_0,
- the number of counts C_0,
- the uncertainty on the number of counts σC_0,
- the uncertainty on the widths σR_x, σR_y

2018-05-09a

run	002-201
cutoff standard deviation	44.5 px
filter conditions	$C_0 > 0$, $\sigma C_0 < C_0/2$, $\sigma R_x < 1px$, $\sigma R_y < 1px$
number of images left after filtering	11703 of 20000

2018-05-24a

run	001-200
cutoff standard deviation	118.1 px
filter conditions	$C_0 > 0$, $\sigma C_0 < C_0/2$, $\sigma R_x < 1px$, $\sigma R_y < 1px$, $150 < x_0 < 700$
number of images left after filtering	11287 of 20000

2018-05-24b

run	202-401
cutoff standard deviation	88.0 px
filter conditions	$C_0 > 0$, $\sigma C_0 < C_0/2$, $\sigma R_x < 1px$, $\sigma R_y < 1px$ $250 < x_0 < 700$,$80 < y_0 < 115$
number of images left after filtering	14353 of 20000

2018-05-24c

run	408-607
cutoff standard deviation	107.6 px
filter conditions	$C_0 > 0$, $\sigma C_0 < C_0/2$, $\sigma R_x < 1px$, $\sigma R_y < 1px$
number of images left after filtering	14742 of 20000

2018-05-25b

run	203-402
cutoff standard deviation	48.2 px
filter conditions	$C_0 > 0$, $\sigma C_0 < C_0/2$, $\sigma R_x < 1px$, $\sigma R_y < 1px$
number of images left after filtering	10636 of 20000

2018-05-25c

run	406-605
cutoff standard deviation	37.6 px
filter conditions	$C_0 > 0$, $\sigma C_0 < C_0/2$, $\sigma R_x < 1px$, $\sigma R_y < 1px$
number of images left after filtering	15553 of 20000

2018-05-25d

run	610-809
cutoff standard deviation	43.0 px
filter conditions	$C_0 > 0$, $\sigma C_0 < C_0/2$, $\sigma R_x < 1px$, $\sigma R_y < 1px$
number of images left after filtering	19400 of 20000

2018-06-01b

run	313-612
cutoff standard deviation	105.2 px
filter conditions	$C_0 > 0$, $\sigma C_0 < C_0/2$, $\sigma R_x < 1px$, $\sigma R_y < 1px$
number of images left after filtering	27074 of 30000

Bibliography

[1] S. Bose, "Plancks law and light quantum hypothesis," *Z. Phys.*, vol. 26, 1924.

[2] A. Einstein, "Quantentheorie des einatomigen idealen gases: Zweite abhandlung," *Sitzungber. Kgl. Akad. Wiss.*, no. 3, 1925.

[3] K. B. Davis, M. O. Mewes, M. R. Andrews, N. J. van Druten, D. S. Durfee, D. M. Kurn, and W. Ketterle, "Bose-einstein condensation in a gas of sodium atoms," *Phys. Rev. Lett.*, vol. 75, pp. 3969–3973, Nov 1995.

[4] S. O. Demokritov, V. E. Demidov, O. Dzyapko, G. A. Melkov, A. A. Serga, B. Hillebrands, and A. N. Slavin, "Bose-einstein condensation of quasi-equilibrium magnons at room temperature under pumping," *Nature*, vol. 443, pp. 430 EP –, Sep 2006.

[5] J. Kasprzak, M. Richard, S. Kundermann, A. Baas, P. Jeambrun, J. M. J. Keeling, F. M. Marchetti, M. H. Szymanska, R. André, J. L. Staehli, V. Savona, P. B. Littlewood, B. Deveaud, and L. S. Dang, "Bose-einstein condensation of exciton polaritons," *Nature*, vol. 443, pp. 409 EP –, Sep 2006. Article.

[6] R. Y. Chiao and J. Boyce, "Bogoliubov dispersion relation and the possibility of superfluidity for weakly interacting photons in a two-dimensional photon fluid," *Phys. Rev. A*, vol. 60, pp. 4114–4121, Nov 1999.

[7] J. Klaers, F. Vewinger, and M. Weitz, "Thermalization of a two-dimensional photonic gas in a 'white wall' photon box," *Nature Physics*, vol. 6, pp. 512 EP –, May 2010.

[8] J. Klaers, J. Schmitt, F. Vewinger, and M. Weitz, "Bose-einstein condensation of photons in an optical microcavity," *Nature*, vol. 468, pp. 545 EP –, Nov 2010.

[9] E. H. Kennard, "On the thermodynamics of fluorescence," *Phys. Rev.*, vol. 11, pp. 29–38, Jan 1918.

[10] B. I. Stepanov, "Universal relation between the absorption spectra and luminescence spectra of complex molecules," *Dokl. Akad. Nauk SSSR*, vol. 112, p. 839âĂŞ841, 1957.

[11] J. Klaers, J. Schmitt, T. Damm, F. Vewinger, and M. Weitz, "Statistical physics of bose-einstein-condensed light in a dye microcavity," *Phys. Rev. Lett.*, vol. 108, p. 160403, Apr 2012.

[12] R. A. Nyman, "Absorption and Fluorescence spectra of Rhodamine 6G," Apr. 2017.

[13] F. van der Laan, "Interaction and polarization measurements of photon bose-einstein condensate," masters thesis, Utrecht University, 06 2017.

[14] P. Kirton and J. Keeling, "Nonequilibrium model of photon condensation," *Phys. Rev. Lett.*, vol. 111, p. 100404, Sep 2013.

[15] P. Kirton and J. Keeling, "Thermalization and breakdown of thermalization in photon condensates," *Phys. Rev. A*, vol. 91, p. 033826, Mar 2015.

[16] J. Marelic and R. A. Nyman, "Experimental evidence for inhomogeneous pumping and energy-dependent effects in photon bose-einstein condensation," *Phys. Rev. A*, vol. 91, p. 033813, Mar 2015.

[17] J. Schmitt, T. Damm, D. Dung, F. Vewinger, J. Klaers, and M. Weitz, "Thermalization kinetics of light: From laser dynamics to equilibrium condensation of photons," *Phys. Rev. A*, vol. 92, p. 011602, Jul 2015.

[18] J. Keeling and P. Kirton, "Spatial dynamics, thermalization, and gain clamping in a photon condensate," *Phys. Rev. A*, vol. 93, p. 013829, Jan 2016.

[19] R. I. Moodie, P. Kirton, and J. Keeling, "Polarization dynamics in a photon bose-einstein condensate," *Phys. Rev. A*, vol. 96, p. 043844, Oct 2017.

[20] H. J. Hesten, R. A. Nyman, and F. Mintert, "Decondensation in nonequilibrium photonic condensates: When less is more," *Phys. Rev. Lett.*, vol. 120, p. 040601, Jan 2018.

[21] S. Greveling, K. L. Perrier, and D. van Oosten, "Density Distribution of a Bose-Einstein Condensate of Photons in a Dye-Filled Microcavity," *ArXiv e-prints*, Dec. 2017.

[22] R. Zondervan, F. Kulzer, S. B. Orlinskii, and M. Orrit, "Photoblinking of rhodamine 6g in poly(vinyl alcohol):âĂĽ radical dark state formed through the triplet," *The Journal of Physical Chemistry A*, vol. 107, no. 35, pp. 6770–6776, 2003.

[23] A. Penzkofer and Y. Lu, "Fluorescence quenching of rhodamine 6g in methanol at high concentration," *Chemical Physics*, vol. 103, no. 2, pp. 399 – 405, 1986.

[24] D. Magde, R. Wong, and P. G. Seybold, "Fluorescence quantum yields and their relation to lifetimes of rhodamine 6g and fluorescein in nine solvents: Improved absolute standards for quantum yields," *Photochemistry and Photobiology*, vol. 75, pp. 327–334, Apr 2002.

[25] K. G. Lagoudakis, M. Wouters, M. Richard, A. Baas, I. Carusotto, R. André, L. S. Dang, and B. Deveaud-Plédran, "Quantized vortices in an exciton-polariton condensate," *Nature Physics*, vol. 4, pp. 706 EP –, Aug 2008.

[26] O. Lahav, A. Itah, A. Blumkin, C. Gordon, S. Rinott, A. Zayats, and J. Steinhauer, "Realization of a sonic black hole analog in a bose-einstein condensate," *Phys. Rev. Lett.*, vol. 105, p. 240401, Dec 2010.

[27] S. Greveling, F. van der Laan, K. L. Perrier, and D. van Oosten, "The Effective Interaction Strength in a Bose-Einstein Condensate of Photons in a Dye-Filled Microcavity," *ArXiv e-prints*, Dec. 2017.

[28] C. J. Pethick and H. Smith, *BoseâĂŞEinstein Condensation in Dilute Gases*. Cambridge University Press, 2 ed., 2008.

[29] H. Alaeian, M. Schedensack, C. Bartels, D. Peterseim, and M. Weitz, "Thermo-optical interactions in a dye-microcavity photon boseâĂŞeinstein condensate," *New Journal of Physics*, vol. 19, no. 11, p. 115009, 2017.